Theoretical and experimental aspects of non-equilibrium plasmas in different regimes: fundamentals and selected applications

11 January 2025

Theoretical and experimental aspects of non-equilibrium plasmas in different regimes: fundamentals and selected applications

Gianpiero Colonna[a,1]**, Carlos D. Pintassilgo**[2]**, Francesco Pegoraro**[3]**, Andrea Cristofolini**[4]**, Arturo Popoli**[4]**, Gabriele Neretti**[4]**, Alix Gicquel**[5]**, Olivier Duigou**[5]**, Thomas Bieber**[5]**, Khaled Hassouni**[6]**, Laura Laguardia**[1]

[1]Consiglio Nazionale delle Ricerche, Istituto per la Scienza e Tecnologia dei Plasmi, Italy
[2]Instituto de Plasmas e Fusão Nuclear, Instituto Superior Técnico, Universidade de Lisboa, Lisboa, Portugal and Faculdade de Engenharia, Universidade do Porto, Porto, Portugal
[3]Physics Department, University of Pisa, Italy and Consiglio Nazionale delle Ricerche, Istituto Nazionale di Ottica, Pisa, Italy
[4]Department of Electrical, Electronic and Information Engineering "Guglielmo Marconi", University of Bologna
[5]DIAM CONCEPT, ACCELÕAIR, 1 Chemin de la Porte des Loges, 78350 Les Loges en Josas, France
[6]LSPM, CNRS - USPN, 99 avenue J. B. Clément, 93430, Villetaneuse, France
Received: date / Revised version: date

Abstract This paper presents recent activities covering different plasma fields, from both theoretical and experimental point of views. An overview of the present interests of the scientific community is reported here. Starting from a brief description of the role of collisions in astrophysical plasmas, some fundamental aspects of gas discharges modelling, such as superelastic collisions and the basic concept of vibrational temperature, are discussed. Different plasma sources, as DBD and microwave discharges with their own specific applications, are reported. Edge plasmas in nuclear fusion reactors are investigated, focusing on the cooling mechanisms resulting from nitrogen puffing in the divertor region.

PACS 52.20.Hv Atomic, molecular, ion, and heavy-particle collisions · 52.25.Dg Plasma kinetic equations · 52.50.Dg Plasma sources · 52.55.Rk Power exhaust; divertors · 52.65.?y Plasma simulation 52.90.+z Other topics in physics of plasmas and electric discharges

1 Introduction

Nowadays, plasma technology has reached a ripeness finding applications in a variety of continuously expanding fields. The intense research activity carried out since the 70's to characterize gas discharges shed light on the mechanisms occurring in the plasma in different conditions and for different mixtures, allowing the development of this technology to the present. Nevertheless, the increasing number of plasma applications is bringing on new problems, consequence of the characteristics of the plasma configuration and of the specific properties of the mixture components.

The main features of the plasma are determined by the interaction with electromagnetic field. However, the specific behaviour of a discharge is determined by the quantum nature of atoms and molecules, emerging in the macroscopic properties of the plasma. The electromagnetic field interacts with charged species, mainly with electrons, due to their small mass relatively to ions, while the plasma properties are often detected from neutrals. The energy is transferred from the fields to neutrals by intermediation of charged particles through collisions.

Depending on the values of specific quantities as electron temperature, electron density, and/or ionization degree, plasmas are usually classified into different categories, joining different communities developing their research in spatial plasmas, thermonuclear fusion, industrial and technological applications, among other important areas.

A rather common classification involves low temperature (LTP), or *cold*, and *hot* plasmas. Gas discharges, a kind of LTP, exhibit unique features, such as different species being described by different temperatures, as shown in section 2.1, the electron temperature be-

[a]e-mail: gianpiero.colonna@cnr.it

ing higher than the vibrational temperature (in molecular gases), in turn, higher than the gas temperature. In the cases here reviewed, the electron temperature is of the order of a few eV (1 eV$\approx$11600 K), while the vibrational temperature is $\approx$5000 K and the gas temperature is $\approx$500 K. These discharges constitute then a physical system out of thermodynamic equilibrium, in which the electrons contain most part of the energy absorbed from the plasma source. Besides these non-equilibrium situations, gas discharges are also characterized by low degrees of ionization, being in general below 10^{-3}. On the other hand, the designation of *hot* plasmas concern usually situations where the electron temperature is much higher than a few eV, and the degree of ionization is $\approx$1. Interestingly, in large devices, as the Tokamak described in section 2 of this paper, the electron temperature at the mid plane of the confined region is $\approx$100 eV, and has quite relatively lower values, 1-2 eV, in the divertor region.

Because of the relative ease with which a cold plasma can be produced on Earth, a great deal of attention has been raised over the decades on the possible employment of such kind of plasmas for a multitude of applications. A prominent feature of cold plasmas is that they can be used to treat surfaces and volumes in both direct and indirect ways [1]. Treatments performed using cold plasmas are also non-destructive and highly energetic [2]. In addition, cold plasmas produce a remarkable number of chemically active species in economically convenient ways [3]. These kind of plasmas are commonly applied in industrial [4, 5], environmental [6, 7], aerospace [8, 9] and medical [10, 11] applications.

The main reason behind the reported vastness and diversity of cold plasma applications lies indeed in the rich physics that characterizes this physical state. The number and complexity of the different phenomena taking place in non-equilibrium plasmas, however, also constitute a challenge from the perspective of understanding, operating and optimizing technologies based on these principles. In this context, considering the high costs associated with prototyping and experiments, the development of reliable tools allowing to perform numerical simulations plays a very prominent role in technological and scientific advancement.

This review collects the contributions presented in the course *Cold Plasmas: Fundamentals and Applications* in the School on Quantum Electronic in Ettore Majorana Center for Scientific Culture in Erice, September 2019, in the topics of *gas discharges* and divertor plasmas. The present paper is composed by seven sections and, according with the course purposes, intends to give an overview of some research activities, spanning from fundamental theoretical aspects to specific applications, focusing on the role of elementary processes and non-equilibrium in determining plasma properties.

The role of collisions is relevant also in systems where usually they are neglected, as discussed in section 2. Collisions are responsible of plasma instabilities and anomalous behaviours, allowing energy transfer from magnetic field to the plasma particles. Part of this section (section 2.1) is devoted to the edge plasma in fusion devices, where the mitigation of the heat flux on the surface is obtained by puffing nitrogen in the divertor region.

In section 3, the self-consistent model considering the synergy between the thermodynamic state (internal distributions) and the free electron kinetics, is presented discussing the relevance of superelastic collisions and of gas temperature profiles in modelling the evolution of gas discharges.

A further contribution (section 4) is devoted to the description of a drift-diffusion model for high pressure dielectric barrier discharges (DBD).

An important DBD application is activated water for sanification. In the case of discharges on the surface of liquid water (see section 5), the production of oxidizing species such as hydrogen peroxide and ozone is efficient, giving to the plasma antiseptic properties.

In section 6 the production of fancy jewels via plasma is presented, focusing on the processes leading to the diamond growth. The tuning of the plasma properties to obtain crystals with the desired characteristics is discussed.

2 High Temperature Plasma Behaviours

Quoting almost *verbatim* from the Introduction of a nearly fourty year old article by R.J. Bickerton [12]: "High temperature plasma physics deals with the behaviour of highly ionized gases. In principle the subject has a stark simplicity since it covers the interaction of structureless charged particles obeying well known physical laws. It is therefore paradoxical that the behaviour of an ionized gas is frequently unpredictable. The subject has its origins in gas discharge physics ionospheric physics and astrophysics. Several key theoretical concepts were developed in connection with these earlier fields; these have been extended and extensively tested experimentally in connection with the thermonuclear fusion and space programmes." When compared with the physics of "cold" plasma discharges, these words point to an obvious difference: the components of a fully ionized plasma are elementary, at least at energies below the threshold for the

production of electron positron pairs and as long as the electromagnetic fields can be treated within the classical Maxwell system of equations, and thus the complexities that arise from the presence of molecules and atoms in different excitation states are absent. The surprise is that, even if the components are simple, their collective behaviour can be extremely complex and can manifest itself in an astonishing variety of forms. As explained in a number of reviews and articles (see e.g. the recent review in Ref. [13]), the plasma collective behaviour and its being generally far away from even local thermodynamic equilibrium can be traced back to the fact that the electromagnetic fields lead to long range interactions that involve particles at distances much larger than the mean particle separation.

In reality in most cases, even in high energy regimes, plasma phenomena include effects that go beyond the fully ionized, weakly coupled plasma paradigm. For example if heavy elements are present, in most cases their nuclei are not stripped of all their electrons. In addition, almost by norm, plasmas are inhomogeneous and colder regions are present even in high temperature plasmas, for example in a magnetic fusion experiment near the walls of the containing vessel. Moreover in dusty plasmas, which are quite relevant for astrophysical configurations, the charge of the dust grain is in itself a dynamical variable so that the physics of electron emission and absorption comes into play.

In fact it is not generally possible to separate completely collisionless from collisional features in a real plasma. The former, the collisionless features, describe the dynamics of fully-ionized, high-temperature, dilute plasmas in the limit where not only atomic processes are absent, but even the effect of purely elastic binary interactions between discrete charged particles (Coulomb collisions) can be disregarded with respect to the collective interaction of the plasma as a whole. In this limit, the discreteness of the charged particles that compose the plasma is immaterial and the electromagnetic interaction can be described in terms of a mean electromagnetic field whose sources are smooth charge and current density distributions. At lower energies collisional effects related to Coulomb collisions can affect the plasma dynamics and at even lower energies, in tens of eV range, atomic and molecular processes and collisions on neutrals play a major role.

A quite scenic example of the interplay between collisionless and collisional effects is provided by the polar aurorae. Quoting from the pioneering article by B. Coppi, G. Laval, and R. Pellat [14]: "For this, we can take up the stability analysis of a collisionless pinch, with the intention to show that the relevant instability has macroscopic effects, as it transforms magnetic

energy into kinetic energy, and that it can be suitable to explain the characteristic times of evolution of phenomena observed during auroral events, in the auroral regions, and in the magnetic tail." Here the authors are referring to the effect of the instability of the antiparallel magnetic field lines in the Earth tail plasma (on the night side of the Earth magnetosphere). This instability goes under the name of magnetic field line reconnection and occurs because of local violations of the ideal MHD condition at special locations in the plasma and in particular where the magnetic field vanishes as is the case at the separation between plasma regions with antiparallel magnetic field lines. Reconnection leads to a large scale rearrangement of the magnetic topology, to the release of magnetic energy and to the production of filed aligned electric fields that can accelerate particles, electrons in particular, to large energies. These violations can occur because of collisional effects (plasma resistivity) or kinetic effects, collisionless by nature, that are described by the Vlasov equation in phase space, as is the case for the process discussed in Ref. [14]: "This occurs through the transfer of macroscopic energy of the plasma to a relatively small number of electrons through microscopic particle-wave resonant processes". The accelerated particles move essentially along the Earth magnetic field lines that extends into the tail and reach the upper atmosphere close to the polar regions where their presence can be detected because of their collisions with the atmospheric neutral constituents. The resulting ionization and excitation leads to the emission of light that appears as luminous drapes of varying colour and intricate folding that can be observed at high latitudes.

An interesting example of the interplay between binary and collective effects in a plasma involves nuclear physics and the possibility to enhance the fusion reaction rate in a strongly magnetized plasma with spin polarized nuclei. Following Ref. [15] we recall that the relatively large cross-section of the reaction

$$D + T \rightarrow {}^4He + n$$
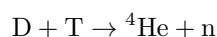
is due to a resonant level of ${}^5He$ with angular momentum $J = 3/2$ which, at the (relatively) low energies of an igniting plasma must arise from the spins of the Deuterons (spin 1) and of the Tritons (spin 1/2). The D-T combined spin states are $S = 3/2$ and $S = 1/2$ while the fusion reaction is due almost entirely to interacting D-T pairs with $S = 3/2$. The statistical weight of this state is two times that of the $S = 1/2$ state. Therefore for a plasma of unpolarized nuclei only 2/3 of the interactions contribute to the fusion rate.

On this basis in 1982 R.M. Kulsrud, H.P. Furth, E.J. Valeo and M. Goldhaber proposed [15] to exploit the

fact that, quoting from their abstract, nuclear "fusion rates can be enhanced or suppressed by polarization of the reacting nuclei. In a magnetic fusion reactor, the depolarization time is estimated to be longer than the reaction time". Important features in this proposal were the (then recent) possibility of producing large quantities of polarized gases and an in depth analysis (see also Ref. [16]) of the processes that could cause a fast depolarization of the polarized nuclei. However in 1983 it was shown in Ref. [17] that an anomalous depolarization process could nevertheless occur because of the onset of a collective instability in the frequency range of the spin precession frequencies of the fusing nuclei. In plasmas in which a considerable fraction of the fusing nuclei are spin polarized, the distribution function of fusion-reaction products turns out to be anisotropic in momentum space and can drive unstable ion cyclotron waves with frequencies close to the spin precession frequencies and cause resonant depolarization at a rate considerably faster than the fusion reaction rate. In Ref. [18] it was concluded that "in a plasma with a spin polarization such that the nuclear reaction rate in enhanced, the tritium nuclei will be depolaraized" under fusion relevant conditions.

It is important to note that the distinction between collisional and collisionless regimes may not be valid uniformly in time, or, more precisely, that the collisionless plasma approximation may cease to be applicable as the system evolves in time. In fact collisionless plasmas are nonlinear Hamiltonian systems with, formally, an infinite number of degrees of freedom. The nonlinear dynamics of such systems is bound to develop increasingly small scales, both in coordinate and in velocity space, making the disregard of collisional effects eventually untenable. This point was stressed in Ref. [19] in the Editorial to a Special Issue entitled "Collisions in collisionless plasmas"' published in 2014 by J. Plasma Physics.

Such a point is particularly evident in the case of the energy cascade in fully developed turbulence from large spatial scales through the inertial range, which at different spatial scales may include different types of collisionless plasma dynamics, down to the dissipative range.

The nonlinear formation of small scales adds an important feature of the interplay between collective and collisional processes in so far as collisional effects can react back on the collisionless dynamics at larger scales and thus affect the features of the particle and field fluctuations that determine most of the macroscopic properties of a plasma.

A transition between hot and cold plasmas can be found in the divertor region of the Tokamak, to moderate the heat flux to the reactor walls.

2.1 Nitrogen Seeding in Tokamak Divertor

One of the most severe problems for future fusion devices is the power load to the divertor target plates [20]. Tungsten (W) is the material decided for the divertor plasma-facing components (PFC_s) from the start of plasma operations for ITER (International Thermonuclear Experimental Reactor). PFC_s in the divertor region will be subjected to very high heat loads from energetic (eV to keV) charged and neutral particle bombardment. In order to avoid W damage, divertor target loads should be kept below 5-10 MWm^{-2} [21] and cooling the plasma before it reaches the divertor is necessary. This can be achieved through the seeding of low Z impurities [22]. Impurity seeding (neutral non-fuel species are puffed into the plasma from gas valves near the divertor region) has been demonstrated to be an effective mechanism both for direct power absorption through multiple ionisations and for the enhancement of radiative power dissipation through inelastic collisions and subsequent relaxations [23].

Typical gases for seeding are nitrogen (N_2) and noble gases like neon (Ne), due to their medium Z number and the desired emission line radiation at temperatures where deuterium (D_2) does not radiate. When the impurities interact with the plasma in the scrape off layer (SOL) they become excited and ionized. By falling back to lower energy states, the difference of energy is radiated away and therefore the temperature in the SOL is decreased. N_2 seeding not only reduces the heat flux onto the divertor but also improves the confinement of the plasma [24].

The impurities have effective emissivities depending on the plasma electron temperature (T_e). While Ne has a cooling potential at a relatively high T_e, and hence may effectively cool the upstream edge plasma, N_2 is effective at the boundary layer, because their emission peaks are located at relatively low values of T_e [25]. However, besides the beneficial cooling, N_2 is also interacting with PFC_s by surface sputtering, ion implantation or chemical deposition, like the formation of tungsten nitrides (WNx) or berillium nitrides (BeN) [26]. This results in a build-up of N_2 content. Additionally, N_2 is chemical active in a hydrogen fuel isotopes environment which leads to the formation of ammonia (NH_3) and other N_2 hydrides [27,28]. The NH_3 formation is a critical issue because, being NH_3 hazardous, might cause damage to pumps, valves and other materials and could have a significant implication on the

operation of the ITER tritium plant which is prepared to process titrated NH_3 in small amounts [29].

2.2 Physics basis for the tungsten divertor

Based on nearly five decades of magnetically confined nuclear fusion plasma physics research, an axisymmetric poloidal magnetic X-point divertor has become the present vision for a tokamak plasma-material interface. In the tokamak, a magnetic X-point is created between two toroidal currents, a plasma current and a special magnetic coil. A formed magnetic separatrix divides the plasma into a closed field line region (confined plasma) and an open field line SOL region. The SOL is directed (diverted) into a special divertor chamber ending on target plates. The poloidal divertor enables energy and particles lost from the confined core plasma due to radial transport and magnetohydrodynamic (MHD) instabilities (e.g., edge localized modes (ELMs)) to flow to the divertor chamber that acts as a separate plasma material interface.

Four tasks are accomplished by the standard poloidal X-point divertor [30]:

1. plasma power exhaust;
2. particle control (D/T and He pumping);
3. impurity production (source) reduction;
4. impurity screening by the divertor SOL.

The divertor SOL parallel heat transport is dominated by electron conduction and convection and strongly depends on plasma collisionality [30–32]. At higher plasma collisionality, a low-temperature highly radiative divertor regime sets in: the plasma flowing to divertor plates loses energy through radiation and dissipative processes (inelastic collisions and recombination) and transfers momentum through charge exchange. This leads to plasma neutralization and detachment from the target plate, and as a result, significantly reduced heat load and material erosion. This regime is commonly called radiative plasma detachment, characterized by a parallel SOL electron (plasma) pressure drop, high neutral divertor pressure (density), low $T_e(\approx$1-2 eV), high electron density (n_e) at the plate and high impurity radiation. This is viewed as the main solution to tokamak power and particle exhaust within operating limits of PFC_s cooling technology and target materials.

The proposed ITER divertor is based on standard X-point geometry designs tested in large tokamak experiments: vertical targets with partial radiative detachment of the strike points are used. The term *partial* here refers to the plasma detachment from the plate only in the radial region adjacent to the separatrix, while the full detachment, highly desirable for impurity erosion reduction, is likely to lead to confinement degradation via an X-point radiative instability.

2.3 Power dissipation in the divertor

The peak heat flux striking divertor target surfaces in future tokamak devices must be reduced from that predicted, based on ELM in H-mode operation of present experiments. The heat flux reduction technique, which has received the most detailed experimental investigation on tokamaks, consists in inducing detachment of both divertor legs and large radiated power in the divertor away from the target plates by strong gas puffing. Frequently the outer leg plasma after gas injection is only detached from the target plates on flux surfaces near the separatrix and remains attached on flux surfaces farther out in the outer leg SOL [33]. This partially detached divertor (PDD) is attractive because the peak heat flux near the separatrix is reduced typically by factors of three-five, which would be sufficient for ITER requirements and an attached plasma remains in the outer SOL from which helium (He) ash could be pumped in a tokamak reactor.

During PDD operations, induced by gas injection, it is possible to distinguish five region, from the midplane to the targets, each dominated by different physics processes: (1) a zone dominated by thermal conduction; (2) a radiation zone; (3) an ionization region; (4) a volume dominated by ion-neutral interactions; and (5) a region dominated by volume recombination. See fig. 1. In a synthetic description of the power exhaust problem the energy dissipation in the plasma edge can be described as a step-ladder process [34]. Power from the confined region (at the mid-plane T_e is $\sim$100 eV) enters the plasma edge by anomalous cross-field transport (turbulent ballooning-like and/or laminar drift-driven) and is mainly conducted along temperature gradients within the SOL. The SOL screens the plasma at the separatrix from thermal neutrals and the energy transport is governed by the conduction along the field line. As the plasma accelerates towards the target plates a fraction of the heat flux is driven by convection and thus may be impacted by plasma drift flows. As energy is transported along the magnetic field lines downstream towards the divertor, it reaches an impurity radiation zone where the temperature is reduced and thus the heat-flux. In the region near the X-point, measurements show high radiation levels during PDD operation. This radiation dissipates energy and T_e is substantially reduced. The measured n_e is not substantially increased so the drop in T_e produces a drop in pressure. Below

the X-point the measured T_e is low enough and the neutral density is high enough so that an ionization region forms. This produces a source which leads to poloidal flow of primary ions toward the target plates.

Farther downstream ion-neutral interactions begin to dominate at low T_e and high neutral density found in the lower part of the outer leg. These collisions can
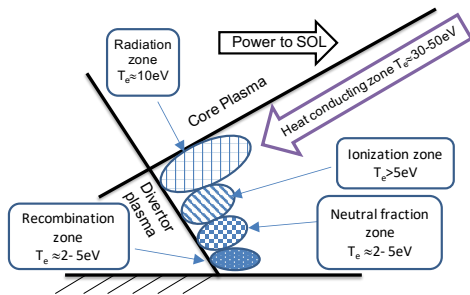

Fig. 1 Schematic diagram for the one-dimensional model of PDD conditions in the outer divertor. Regions dominated by radiation near the X-point, ionization and recombination and ion-neutral interactions are shown. Conduction dominates the energy transport above the X-point; convection dominates below the ionization region.

remove parallel momentum across the field lines from the plasma flow. This effectively reduces the flow velocity toward the target plate. For the region in which the flow velocity is low enough that the transit time through a volume is comparable with the recombination time, substantial recombination takes place. This occurs in the volume above the target surfaces and effectively reduces the ion current striking the plates near the outer strike point (OSP) to substantially lower values than in the attached plasma conditions. The combination of low ion current recombining at the plate and reduced energy transport to the plate, due to the high radiation near the X-point, produces the observed low peak target heat flux near the separatrix strike point.

2.4 Power dissipation by radiation losses

Normally impurity particles enter the plasma as neutral particles, being generated in erosion processes of the wall elements [35, 36] or deliberate puffed [37]. The processes of ionization and recombination convert these neutrals into ions with different charges Z. The energy associated with impurity radiation is lost through three main channels: line emission, bremsstrahlung, and radiative recombination. The power density of radiation losses from all impurity charge states, in coronal equi-

librium, can be calculated as follows [38]

$$Q_{\mathrm{rad}} = \sum_z n_e \, n_z L_z \qquad (1)$$

Here n_e is the density of plasma electrons which lose their energy either by exciting electrons bounded in impurity ions or by elastic coulomb scattering, n_z the density of impurity ions of the charge z and L_z the radiative efficiency. In coronal equilibrium in which the charge state distribution is governed by the balance between ionisation by electron impact and radiative recombination, L_z is a function of the T_e only. L_z of N_2 [39] has a maximum at low temperature and, therefore, is a suitable choice as edge and divertor radiator. At the plasma edge, where steep gradients exist and ELMs [40] take place, the local coronal equilibrium cannot be established. This situation is denoted as non-coronal equilibrium and affects the edge radiation of low-Z impurities. In this case, the radiative loss function is not only a function of the temperature but also of the residence time [41].

Equation 1 is valid under the following assumptions: the characteristic ionization and recombination times are longer than the times of natural radiative decay of the excited states, n_e is such that the mixing of the neighboring levels is unimportant, the electromagnetic fields do not allow forbidden lines to be emitted, etc. If these assumptions, or some of them, are not satisfied, then it is necessary to construct a complete collisional-radiative model in which the deviation of the electron distribution function from being Maxwellian should generally be taken into account.

2.5 Nitrogen seeding experiments

With the coming of all metal devices, understand the behaviour of N_2 and NH_3 have become a priority for ITER and this point was addressed in the EUROfusion work program "Preparing an efficient operation of the PFC for ITER and DEMO". Thereby potential safety and operational issues for ITER have been identified and studied, in tokamak as well as in laboratory experiments, to evaluate the applicability of N_2 as seeding gas in future nuclear fusion devices.

Important questions to solve are the following: how much of the puffed N_2 is interacting with the plasma and therefore makes a contribution to radiation cooling? Is it possible to link this puffed/interacting N_2 with the production of NH_3? How much N_2 is retained upon implantation onto plasma face components?

Experiments performed in tokamak have answered essentially at the first question, instead laboratory experiments of the plasma wall interaction have tried to answered at the last two questions.

2.6 Nitrogen seeding experiments in tokamak: the radiated power fraction

High radiation scenarios with N_2 impurity seeding were tested at two of the all-metal tokamaks, ASDEX Upgrade (AUG) and JET. These experiments were aimed at demonstrating the power exhaust at the highest heat fluxes. The dominant parameter determining these heat fluxes is the ratio of the power flux over the separatrix P_{sep} and the major radius of the plasma R [42].

The radiated power fraction in AUG ($f_{rad} = P_{rad}/P_{heat}$) in discharges where 18MW of heating power are applied at a constant N seeding rate is around 75%, while in discharges with lower heating power up to 90% of the heating power is radiated in the detached state.

At JET where also 18 MW of heating power were applied at constant N seeding rate, with divertor in a fully detached state, a radiated power fraction of about 75% was achieved, the maximum observed at JET [43]. At a higher heating power (27 MW), the plasma showed values of confinement and radiated power fraction similar to those measured at 18 MW.

For both devices, in N seeded detached discharges, the dominant radiation is emitted by a small region inside the confined region, above the X-point. In both cases, about 5 MW are radiated from this region, which is about 40% of the total radiation for JET and AUG.

In AUG constant seeding leads to a slow increase of the N concentration in the confined plasma due to the residence time of N_2 in the vacuum chamber. The X-point radiator moves upwards inside the confined region with the increasing of the N concentration. It appears to be very localized and not significantly elongated along the magnetic field lines. The intense radiation in this region indicates a strong reduction of the local temperature where N_2 radiates efficiently. Electron temperatures of only a few eV are indicated by the SOLPS modeling and by the observation of D_2 line radiation in the region below the X-point radiator. However, no direct measurement of T_e in this region is available yet. The local reduction of T_e could represent the so-called *radiation condensation*: the impurity radiation cools down the plasma towards the temperature of the most efficient emission, leading to the increase of the density in this region and to a further amplification of the radiation losses. The X-point radiator is observed in both devices, at AUG and JET, indicating that it

is a general operational regime for devices with a full-metal wall. For both devices the radiator is, in detached conditions, inside the confined region and dissipates a significant fraction of the injected power. Therefore the injection of N_2 impurity in the plasma converts the heat flux into electromagnetic radiation and redistribute it over the whole plasma vessel surface [44, 45].

2.7 Nitrogen seeding experiments in laboratory: formation of nitrides and ammonia by plasma wall interaction in GyM linear device

Global gas balance experiments at ASDEX Upgrade (AUG) and JET have shown that a considerable fraction of N_2 injected for radiative cooling is not recovered as N_2 upon regeneration of the liquid helium (He) cryopump. The most probable loss channels are ion implantation into plasma-facing materials, co-deposition and NH_3 formation. These three mechanisms were investigated in laboratory experiments performed in linear device [46–50]. Linear devices have extensively contributed to understand the atomic and molecular processes led by N_2 injection, because of the good diagnostic accessibility and the capability of maintaining the plasma in steady-state regime for long time.

Here we present results in term of the N_2 conversion in NH_3 and N_2 interaction with W, obtained in GyM during the last five years N_2 seeding experiments. A detailed description of the design of the machine together with its capabilities can be found in ref. [51]. In short, GyM is a linear plasma device consisting of a cylindrical vacuum vessel (R=0.125 m, L=2.11 m) mounted in a linear magnetic field (up to 0.13 T on the axis), in which highly reproducible plasmas are obtained and steadily sustained by continuous wave microwave power (3 kW, 2.45 GHz). A dedicated sample-introduction system was designed and installed in such a way that the samples are located at the center of the plasma column (20 cm of diameter) and exposed normally to magnetic field lines.

Experiments devoted to ammonia quantification were performed keeping constant the N_2/D_2 partial pressure ratio at 10% and varying the N_2 concentration from 2% to 10%; in these conditions the neutral plasma pressure varied from 2.0×10^{-2} Pa to 5.5×10^{-2} Pa. The main plasma parameters were T_e=5 eV and n_e=2×10^{16} m^{-3} as measured by Langmuir probe at the center of the plasma column. The purpose of the experiments, in addition to quantify ammonia produced as a function of the N_2 concentration was to identify which factors (isotope effect, noble gas injection, metal wall) can limit ammonia formation.

Differentially pumped Quadrupole Mass Spectrometer (QMS) and Optical Emission Spectroscopy (OES) diagnostics were both used during the experiments for qualitative analyses of gas species and radicals resulting from the plasma. In particular, OES detects the emission bands of ND radicals at 335.7 nm and 336.4 nm. Assuming that these signals come from ammonia formation, band intensity can be used as an indicator of how much ammonia is produced during the experiments. In order to quantify the ammonia produced, the exhaust from GyM vessel was collected by a liquid nitrogen trap (LN trap). Ammonia contained in LN trap was then counted by a chromatographic system [52]. In fig. 2 a typical OES acquired in the range between 320-350 nm, is shown.
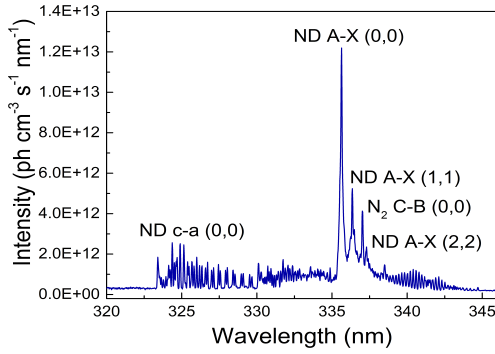

Fig. 2 OES spectrum emitted from ND, belonging to $A^3\Pi - X^3\Sigma^-$ system for the transition (0,0) and (1,1) respectively, and N_2, belonging to the first positive system $B^3\Pi_g - A^3\Sigma_u^+$ for the transition (0,0). Reproduced from Ref. [50].

It is possible to distinguish three different signals: two distinct bands emitted from ND radicals at 335.7 and 336.4 nm and one emitted from N_2 molecules at 337.13 nm. ND signals belong to $A^3\Pi - X^3\Sigma^-$ system for the transition (0,0) and (1,1) respectively. The N_2 signal belongs to the first positive system $B^3\Pi_g - A^3\Sigma_u^+$ for the transition (0,0). The presence of these radicals and molecules is a fingerprint of chemical reactions occurring either in the plasma or at the vessel wall with ND_x as reaction intermediates [53].

In fig. 3 a typical QMS spectrum acquired during an N seeded D plasma experiment in GyM is shown.

QMS is connected to the GyM vessel by a 4mm pipe. Connection is located at 30 cm from the power source and analyse the neutral gas composition flowing into spectrometer from the plasma column. During the discharges, the intensities at the following discrete mass-to-charge ratios were recorded: 2, 3, 4, 12, 13, 14, 15, 16, 17, 18, 19, 20, 21, 23, 28, 29, 30, 31, 32 and 44 AMU/e. The 2-4 AMU range is expected to be populated by D_2 species, the 15-20 AMU range is expected to be popu-
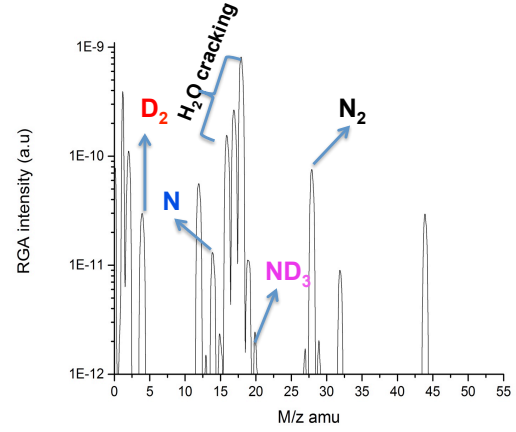

Fig. 3 Typical RGA spectrum acquired during an N seeded D plasma experiment in GyM.

lated by ammonia, water (H_2O) and methane (CH_4) in H and D isotope configurations. Mass 28 AMU is expected to be populated primarily by N_2 (with a smaller signal at 14 AMU), but also by CO. Mass 32 AMU is attributed to O_2.

Time-integrated intensities of the masses N, N_2, D_2, ND_3 were recorded to analyse the evolution of the chemical species during the different phases of the experiment (background vacuum, gas injection, plasma on and plasma off), as reported in fig. 4
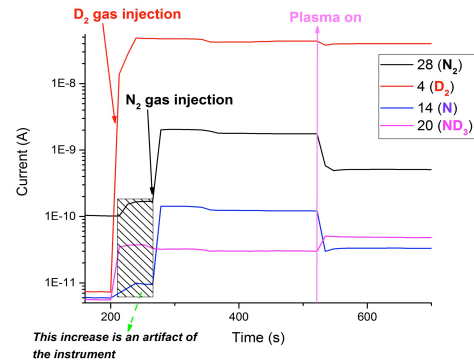

Fig. 4 Mass to charge signals versus time during N_2/D_2 plasma in GyM device. Reproduced from Ref. [52].

During the N_2 gas injection phase the signal of 20 AMU, which corresponds only to ND_3 (no deuterated H_2O or CH_4 were detected during the control experiment) does not increase, while it grows up at the plasma switch-on while at the same time intensity of 14 and 28 AMU of N and N_2 decreases, highlighting that ammonia is formed only during the plasma phase.

Quantitative LIC (Liquid Ion Cromatography) analysis of the exhaust collected is reported in fig. 5, which shows that ammonia conversion decreases from 30%

to 10% as the total pressure increases from 2×10^{-2} to 6×10^{-2} Pa. Such a decrease is in line with the results obtained in reference [54], where model calculations showed a decrease of the ammonia concentration in the plasma as pressure increases.
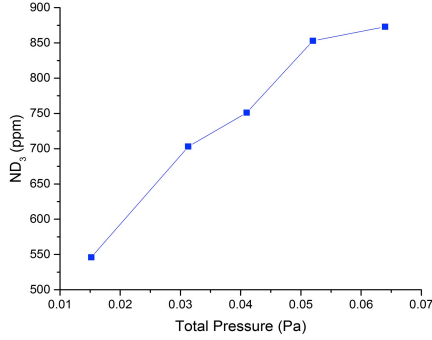

Fig. 5 Ammonia conversion as a function of the total neutral pressure of N seeded D plasmas. Reproduced from Ref. [52].

Moreover it was noticed that ammonia conversion increases from 12% to 17% with the T_e in the range of the 3 - 6 eV [52]. This effect is expected independently from the chemical mechanism involved in the ammonia formation because, at higher T_e, molecule excitation and dissociation increase, as well as the probability that excited chemical species react with a consequent larger production of ammonia. It is known [55, 56] that ammonia formation in low-pressure N_2/D_2 microwave discharges, where D_2 concentration is greater than 50%, can be explained by the formation of ND radicals in the plasma volume and their diffusion to the wall. Here the ND radicals absorbed on the surface continue the reaction path leading to the formation of ammonia. The metal wall acts as a catalyst and, since precursors are produced in the plasma volume, the mechanism responsible of the ammonia formation in devices with metal wall is called *plasma catalysis*. As described in Ref. [57], plasma catalysis involves mainly radicals and vibrationally excited species.

Although a kinetic model able to explain the most probable mechanism leading to the ammonia formation in GyM during N_2 seeding experiments is still missing, ND radical generated in plasma volume can be considered the precursor of the ammonia production.

In order to identify a method to reduce or prevent ammonia formation during experiments with N_2 seeding in plasma devices, the effects of argon (Ar) and Heinjection at the N_2/H_2 mixture were also evaluated in GyM. Figure 6 shows ammonia conversion in the following conditions (expressed in terms of molar concentrations): (i) 96.3% D_2 + 3,7% N_2 , (ii) 79.8% D_2 + 3,2% N_2 + 17% He and (iii) 93.4% D_2 + 3,2% N_2 + 3,1% Ar.
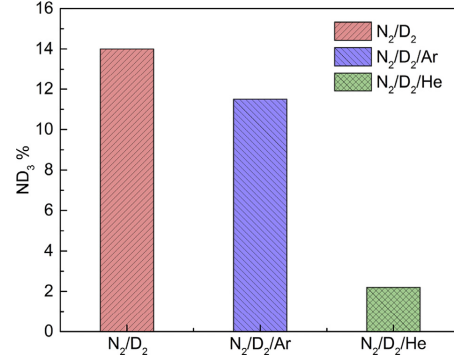

Fig. 6 Ammonia conversion during N_2/D_2, $N_2/D_2/Ar$, $N_2/D_2/He$ plasmas. Reproduced from Ref. [52].

It is evident that He reduces ammonia production while Ar seems to be practically not effective. Comparison of OES measurements for the three experiments evidences that the content of nitrogenized species and the D_2 dissociation is unchanged adding Ar or He, indicating that the interaction between N_2 and D_2 in the plasma phase is not affected by noble gases addition. The overall analysis of the LIC and OES measurements suggests that this reduction of the ammonia formation could be ascribed to a variation of the chemical-physical processes occurring on the surface of the wall. Thus, to explain the observed reduction in ammonia formation during discharges in He, we propose that He is prone in metals to create surface modification acting as a barrier for D_2 adsorption. This has been observed for W and molybdenum (Mo) in the fusion community [58]. The metallic wall of GyM is no longer a reservoir of D_2, required for the production of ammonia by a catalytic surface reaction, once the He is adsorbed. The change of the seeding species from He to Ar supports this statement, as Ar does not lead to this kind of surface modification [59, 60].

In order to study W surface modifications (chemical and morphological) during N_2 seeding experiments, samples, different in crystalline domain size, crystallographic phase and composition, have been simultaneously exposed to N_2/D_2 plasmas. The samples were located at the center of the plasma column (20 cm of diameter) and exposed normally to magnetic field lines. To better identify the nature of the interactions of N and D species with W, experiments were carried out with and without negative bias potential on the substrate even at very high temperatures. After plasma exposure, the specimens were characterised by profilom-

etry, X-ray depth-profiling photoelectron spectroscopy (XPS) and atomic force microscopy (AFM).

The results of the profilometry measurements demonstrated that W erosion depends of the bias applied and, above all, on the structure and composition of the exposed samples.

Investigations of the N_2/D_2 plasma exposure effects on the W films morphology, performed by proper diagnostics, revealed no evidence of blisters formation on the surface of W samples and an evident change of the morphology. The change in surface morphology depends mainly on the structure of the exposed samples while no substantial change in morphology is evident with the change in bias and fluence.

Chemical modification of the surface W samples after exposure at N_2/D_2 plasmas were investigated by XPS. In fig. 7 are shown the high-resolution XPS spectra of N1s and W4f electrons of the samples exposed at N_2/D_2 plasma without bias applications. At their surface three contributions under W4f line have been resolved via deconvolution while two contributions are well resolved under the N1s line. Under the N1s line, WNx bonds was assigned at 397.4 eV of binding energy (B.E.) and the corresponding one under the W4f line at 31.42 eV of B.E. A contribution due to N retained at W grain boundaries was assigned at 400.3 eV in B.E under the N1s line and at 33.15 eV in B.E under W4f line [61].

Differences in N relative concentrations along the depth, have been found for the samples [50]. The thickness of the layer in which N_2 is retained is about 6 nm. Below 6 nm the N1s line was no longer detected. Because the samples were exposed to the same discharges, the differences found in the N_2 concentration are ascribed to their different strucures. W4f core level of all the samples exposed to plasma with bias application shows the same contributions observed in samples exposed to N_2/D_2 plasmas without bias. Instead bias application produces a substantial modification of the N1s signal. The XPS spectra of N1s electrons observed on the W substrate exposed to plasmas with bias are shown in fig. 8.

After exposure of the W substrates to the N_2/D_2 plasma, spectra of N1s core level presents contributions of the five species: W_2N, WN, ND, ND_2 and ND_3 bound to W with a different number of coordination sites maintaining the valence of N constant. Evidence of these bondings was observed in case of transition metals used to synthesise ammonia [53, 62, 63]. While the ND_x peaks were detected only at the surface, the W_2N and WN contributions survive up to 16.5 nm. When the negative bias potential was applied on the W substrate, the peaks due to the adsorbed species N,
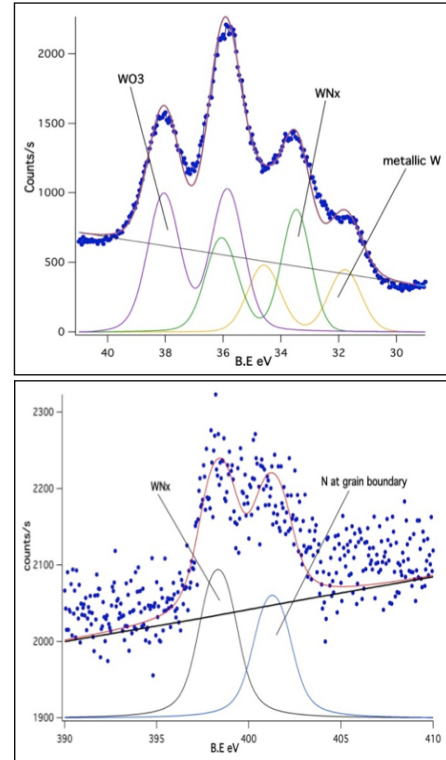

Fig. 7 Deconvolution W4f line and N1s line of W sample. Reproduced from Ref. [50].

ND, ND_2, and ND_3 decreased with increasing negative bias potential.

3 Self-consistent model and superelastic collisions

For low temperature ionized gases, the perspective is reverted with respect to high temperature plasmas. In this case, the main features of the plasma are determined by the collisions, not by co-operative behaviours as described in the previous section. Usually, a cold plasma is globally neutral, but at short distances, of the order of the Debye length, non-neutrality exists. This condition is described by the Vlasov equation [64], which couples the collisionless Boltzmann and the Poisson equations. A self-consistent field arises, balancing electrostatic forces and particle thermal diffusion. In low-pressure discharges this behavior is revealed in the sheath , the non-neutral region formed in the vicinity of the electrodes, responsible of the voltage drop in the plasma bulk. Moreover, the plasma modifies also the electrostatic interaction at atomic length scale and the charge interaction is ruled by the screened Coulomb (or Yukawa) potential [65], modifying the level energy and the effective number of bounded levels [66]. This aspect is important not only for the determination of the
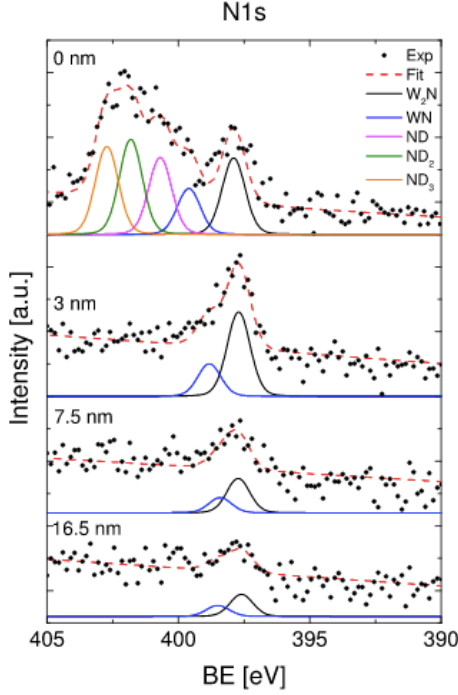
Fig. 8 N1s core level XPS spectra of the surface and sub-surface layers of a film exposed in GyM at a bias voltage of 100 V. Reproduced from Ref. [49].

thermodynamic and transport properties of dense plasmas [67,68], but also for their chemical properties, such as the rate coefficients that depend on the population distribution of the excited states, which could be far from equilibrium.

In general, to describe non-equilibrium distributions of atomic levels collisional-radiative models have been developed. The evolution of the collisional-radiative model is the state-to-state approach, extending the kinetics also to vibrational and electronic states of molecules. A further step in growing the complexity of low-temperature, non-equilibrium plasma modelling is to consider the electron distribution function departing from a maxwellian. This characteristic, commonly accepted by the community and verified experimentally, is the consequence of inelastic collisions and reflects on the rate coefficients, which, deviating from the Arrhenius trend, depend on the thermochemical state of the gas [69]. To model non-equilibrium electron distributions, the Boltzmann equation must be solved. A suitable approach, if the electric field is not too high, consists in the two-term approximation [70] where the distribution is considered the sum of isotropic (f_0) and anisotropic ($\vec{f}_1$) parts, function of the electron energy ε

$$f_e(\vec{r},\vec{v},t) = f_0(\vec{r},\varepsilon,t) + \vec{v} \cdot \vec{f}_1(\vec{r},\varepsilon,t) \qquad (2)$$

where f_0 is known as *electron energy distribution function* (eedf). This model is the first order approximation of the spherical harmonic expansion, and in some conditions, multi-term extension is considered [71–73], at the cost of the computational time. As an alternative, Monte Carlo approaches [74] can be used, which is equivalent to calculate the full series expansion. With some exceptions [75], the two-term Boltzmann equation is applied to characterize the electron gas in the bulk of the plasma, where the gradients of the distributions are small, and the assumption of a homogeneous discharge is accurate enough, allowing to neglect spatial gradients in the calculations. In the two-term approximation, assuming that f_1 reaches the stationary value in a time much shorter than the isotropic part, the equation for f_0 becomes [76]

$$\frac{\partial f_0(\varepsilon,t)}{\partial t} = -\frac{\partial J_f(\varepsilon,t)}{\partial \varepsilon} - \frac{\partial J_{el}(\varepsilon,t)}{\partial \varepsilon} - \frac{\partial J_{ee}(\varepsilon,t)}{\partial \varepsilon}$$
$$+ S_{in} + S_{sup} \qquad (3)$$

where J's are energy fluxes due to the fields (J_f), elastic collisions with heavy particles (J_{el}) and electron-electron collisions (J_{ee}) while S's account for jumps in the energy space due to collisions. In particular S_{in} includes inelastic transitions (excitation) and S_{sup} superelastic or second kind (de-excitation) collisions. All the terms depend on the gas composition and on the internal structure of the mixture components. The anisotropic part can be calculated from f_0 and its derivatives. Detailed description of J and S can be found in refs. [70, 77].

Known the eedf, it is possible to calculate the rate coefficients K_p, of a generic process p, integrating the corresponding energy-dependentcross section σ_p as following

$$K_p = \int_{\varepsilon^\star}^{\infty} f_0(\varepsilon)v(\varepsilon)\sigma_p(\varepsilon)d\varepsilon \qquad (4)$$

where $v(\varepsilon) = \sqrt{\frac{2\varepsilon}{m_e}}$ is the electron velocity and the normalization condition

$$\int_0^{\infty} f_0(\varepsilon)d\varepsilon = 1 \qquad (5)$$

holds. From the eedf it is possible to calculate also the transport properties [78], such as electron mobility and diffusion, even if to increase the order of approximation multi-term approach must be used [79, 80]. All these data are necessary to model the plasma properties. It is worth to emphasize that some stationary Boltzmann
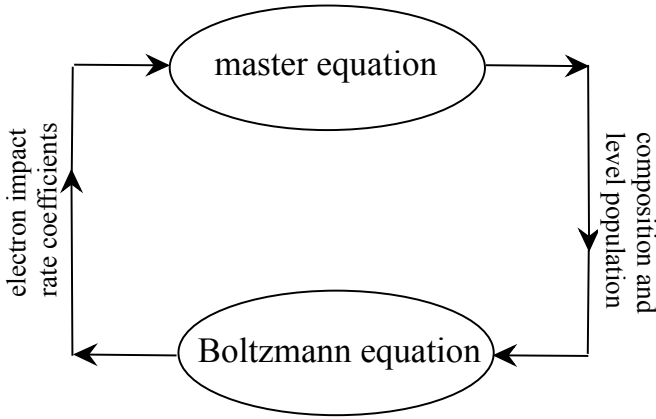
Fig. 9 Simplified scheme of the self-consistent approach. Together with the population, also pressure and temperature are passed to the Boltzmann solver, while together with the rate coefficients, also electron diffusion coefficient is passed to the master equation.

Fig. 10 Plasma density (n_e) and electron temperature (T_e) as a function of different field frequency neglecting (G) and considering (M) processes starting from excited states in Argon discharges. The discharge is obtained with a parallel plate with a gap of 3.2 cm, peak voltage drop of 100 V and gas pressure of 100 mTorr. Data from ref. [107].

solvers, such as LOKI-B [81] and BOLSIG+ [82], are freely available.

In many cases the concentration of the major species in the plasma remains practically unchanged and the characteristic time of eedf relaxation is much shorter than the one of the chemical composition. In this conditions the eedf is only a function of the reduced electric field (E/N) and the rate coefficients and swarm data can be tabulated as a function of E/N [83,84] or of the electron mean energy ($\bar{\varepsilon}$) [85,86], a monotonic function of E/N. The electron properties are tabulated versus $\bar{\varepsilon}$ [85] or electron temperature (T_e) [86], decoupling electron and chemical kinetics. Moreover, these approaches neglect also collisions involving excited species, from this the name *ground state models*. The limits of validity of ground state models have been investigated by different authors, for example focusing on errors made in the I-V characteristic in He discharges [87] or on the effects of strong gradients of the electric field [88].

To overcome the limits of the ground models one should consider the self-consistent state-to-state (SC-StS) approach [89–92]. It consists in the solution of the time-dependent Boltzmann equation for free electrons and the master equations for chemical species and level population, as depicted in the simplified scheme in Fig. 9. This model, determining at the same time the eedf and the thermodynamic state of the plasma, allows to consider variations in the plasma composition, electron-electron collisions and electron induced processes from excited states of atoms and molecules. This approach has been applied to atomic systems [93–95], to molecular plasmas [96–100], also to evaluate the effects of using complete sets of vibrationally-resolved cross sections [101,102], and to complex mixtures [103–106].
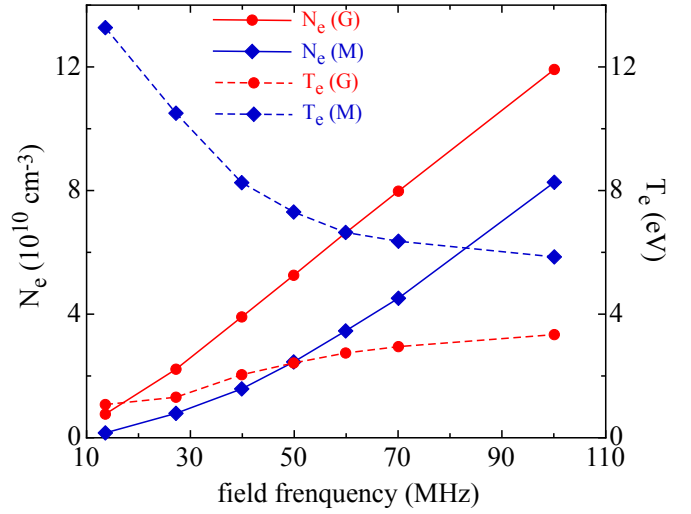
As an example, Sharma et al. [107] discusses the effects of metastable state kinetics in a high frequency parallel-plate Argon discharges, modelling the system with 1D PIC (Particle In Cell) MCC (Monte Carlo Collisions) code. In particular the paper is focused on the role of processes involving metastable excited states in affecting the plasma properties as a function of the applied field frequency. In Fig. 10 it is reported the comparison between the ground and self-consistent model, where the former neglects and the latter includes the kinetics of metastable states. For the electron density the difference between the two cases are quantitative, with the ground model predicting higher values than the self-consistent, even if both models show growing trend with respect to the field frequency. Different behaviours are obtained for the electron temperature. While in the self-consistent case the electron temperature decreases with increasing the frequency, the opposite trend is observed in the ground model, showing a sigmoid shape that reaches an asymptotic value smaller than in the self-consistent results. The higher T_e in the self-consistent case is probably due to the lower electron density, modifying the Debye length which causes a larger potential drop in the sheath region.

Transitions starting from excited levels are even more important in molecular systems , due the the small value of the vibrational quanta. In particular, the use of a cross section sets considering the full transition matrix for the vibrational excitation and chemical processes starting from vibrationally excited states have been investigated for O_2 [108], N_2 [101], H_2 [102,109]
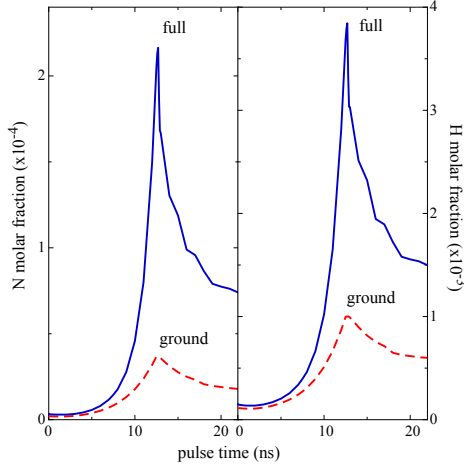
Fig. 11 Nitrogen and Hydrogen atom molar fraction in a multi-pulse N_2/H_2 (1:1) atmospheric pressure discharge. The time is relative to the beginning of the fourth pulse. Data from ref. [106].

Fig. 12 Steady state eedf in an He plasma calculated at E/N=2 Td for [He(^{3}S)]/[He(^{1}S)]=10^{-6} (solid line) compared with the Maxwell distribution at the same temperature (dashed line). The arrows indicate the jump of electrons in the energy space due to superelastic collisions with He(^{3}S) metastable where $\varepsilon^\star = 19.82$ eV is the threshold energy marked. Data from ref. [116].

and N_2/H_2 [106] discharges, for the last system, as an example, let us present the molar fraction of atomic species (see Fig. 11). Two models have been compared, the *ground*, including only excitation from the ground state, and the *full*, including the transitions starting from all vibrationally excited level of the ground electronic state. In this case, the atom density is higher in the full model than in the ground. The full model transfers more energy to the vibrational degrees of freedom, enhancing the dissociation from vibrationally excited states.

The main feature of the self-consistent approach is to include in the calculation the superelastic collisions [110–115], the reverse of the of inelastic processes

$$X_\ell + e(\varepsilon) \rightarrow X_{\ell' < \ell} + e(\varepsilon + \varepsilon^\star_{\ell', \ell})$$

where X_ℓ is the species X in a specific state, being ℓ an ordering number for growing level energy, ε is the electron energy and $\varepsilon^\star_{\ell', \ell}$ the threshold energy of the transition. Their effect is to make the electrons gain the energy lost by internal state when decaying in a level at lower energy, with the consequence of overpopulating the eedf tail. In recent years some investigations have been dedicated to deduce rules to predict the effects of superelastic collisions in noble gas discharges [116], being clearly visible due to the large threshold energy. This behaviour has been sketched in Fig. 12 where the stationary eedf calculated for a fixed fraction of Helium metastable state is compared with the Maxwell distribution at the same mean electron energy. Long plateaux appear at multiples of the threshold energy. The mechanisms of formation of such plateaux (see Fig. 12) are the following: due to superelastic collisions, a peak is
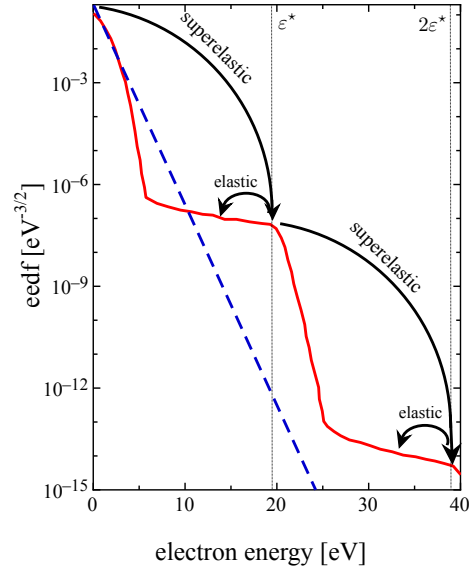
formed at the threshold energy in a very short time. The electrons of the first peak are in turn subjected to superelastic collisions, creating a second peak, and so on. In the longer time, elastic collisions fill the holes between the peaks, forming the plateaux.

This simple chain of processes becomes more complex for mixtures, where the cooperation of inelastic and superelastic collisions with different species creates a series of peaks and valleys in the eedf, as it was observed in the $He/CO_2/CO/N_2$ laser [117]. The effect of superelastic collisions is amplified when coupled with electron-electron collisions, in both discharges [69, 118] and high enthalpy flows [119]. The superelastic collisions are important also for vibrational transitions, acting on the eedf as an additional electric field [117], due to the small threshold energy.

The above considerations are referred to the eedf when all the other quantities are kept constant. However, when the self-consistent approach is used, strong non-linear coupling between the eedf and the internal distributions makes the plasma evolution more complex, especially if the electric field is calculated from the power density w absorbed by the plasma

$$w = \vec{J} \cdot \vec{E} = n_e \mu_e E^2, \tag{6}$$

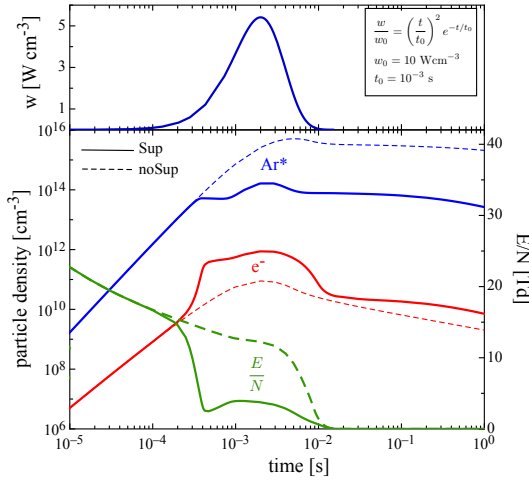or if a plasma is inserted in a polarization circuit

Fig. 13 Temporal profile of the applied power density (upper graph) and the resulting electron and Argon metastable density and reduced electric field, including (Sup) and neglecting (noSup) superelastic collisions in the Boltzmann equation. Data from ref. [120].

Fig. 14 Electron mean energy ($\bar{\varepsilon}_e$ (upper graph) and mobility (μ_e) as a function of the reduced electric field profile including superelastic collisions in the Boltzmann equation in an Argon discharges. The arrows indicate the direction of time. Data from ref. [120].

$$\frac{E}{N} = \frac{E_G}{N} \frac{1}{1 + n_e \mu_e \tilde{R}}, \tag{7}$$

where E_G is the field produced by the power supply in the absence of current and $\tilde{R}$ is the reduced circuit resistance, depending also on some geometrical parameters of the discharge [120].

In this case the electric field (E) depends on the current density (J) i.e. on the electron density n_e and mobility (μ_e), which are a function of the electric field. This non-linear coupling makes the interplay between the different actors unpredictable a priori and numerical calculations are necessary.

To evaluate the role of superelastic collisions in the electron kinetics, in ref. [120] results obtained with the self-consistent model considering (Sup) or neglecting (noSup) superelastic collisions in the Boltzmann equation, but considering the complete model in the level kinetics, are compared. Two systems are considered, an Argon discharge with a given power profile and a Nitrogen discharge with a polarization circuit. Neglecting superelastic collisions only in the Boltzmann equation reproduces the main features of the local field approximation [83, 84]. It should be noted that the relevance of superelastic collisions in determining the eedf during the post discharge is commonly accepted, but usually neglected during the discharge, considering the eedf determined by the electric field, elastic and inelastic collisions. As an example, let us discuss the results in ref. [120] for the Argon discharge. Fig. 13, comparing the temporal profile of the self-consistent field and of electron and metastable state density in the
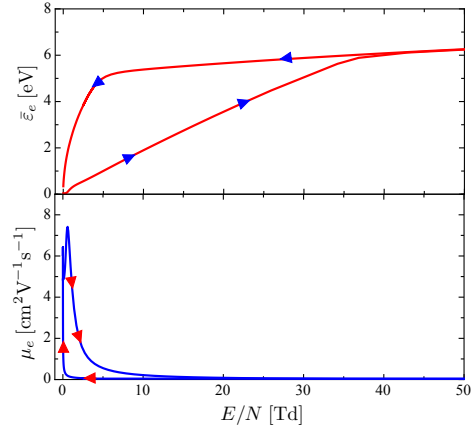
Sup and noSup cases, shows that also during the discharge superelastic collisions have an important effect. The metastable density is lower in the Sup case than in the noSup, while an opposite trend is observed in the electron density, a behaviour reflected on the electric field. Including the superelastic collisions in the Boltzmann equation results in the balance between inelastic and superelastic collisions and as a consequence a given transition become transparent to electrons. Therefore, the eedf is higher at the threshold of ionization, giving higher ionization rates and then higher electron density, in spite of the fact that the electric field is smaller in the Sup case.

The mutual dependence of reduced electric field and mobility (see Eqs. 6,7), considering also the contribution of superelastic collisions and the dependence of such quantities on the metastable density, has the consequence that the swarm parameters are not a monotonic function of the electric field. In fact, as can be observed in Fig. 14, both the mean energy ($\bar{\varepsilon}_e$) and electron mobility μ_e describe a hysteresis loop when reported as a function of the effective electric field.

Besides the necessary inclusion of the effect of superelastic collisions in the solutions to the electron Boltzmann equation, a SC-StS approach enables the determination of the densities of the most important excited species, including electronically as well as vibrationally excited states in the case of molecular plasmas. This kind of information gives more insight into the overall plasma chemistry, providing at the same time additional and important information about the different power transfer channels involving the energy absorbed by the electrons from the electric field. Just to give some examples, nanosecond pulsed discharges in air are

known to play an important role in combustion and gas heating due to the energy stored in the electronically excited states of O_2 [121], whereas the relaxation of the vibrationally excited molecules of nitrogen in the afterglow of pure N_2 discharges is found to be responsible for the formation of the so-called *pink afterglow* [122, 123] downstream from the discharge.

In the case of molecular gases, once the densities of vibrationally excited molecules are known, it is usual to consider a *vibrational temperature* to describe the degree of vibrational excitation. This parameter has different definitions in the literature. In diatomic molecules, such as N_2, O_2, or H_2, this quantity is traditionally determined from the first two vibrational levels of the electronic ground state, usually described as the first level vibrational temperature, given by $T_{0,1} = E_{0,1}/\ln(N_{v=0}/N_{v=1})$, where $E_{0,1}$ represents the energy difference between vibrational levels $v = 1$ and $v = 0$ expressed in K, with densities $N_{v=1}$ and $N_{v=0}$ [124].

In other works, the vibrational temperature is defined as the characteristic vibrational temperature of a Treanor-like distribution that best fits the densities of a predefined number of vibrational levels. For instance, in N_2 or O_2 discharges, a fit over the first four vibrational levels is often considered [125]. Moreover, recent modelling works dealing with vibrational kinetics in non-equilibrium air plasmas produced by shock waves [126] and hypersonic flows [127] consider a vibrational temperature determined from the solutions to the following equation:

$$\frac{\sum_v E_v N_v}{\sum_v N_v} = \frac{\sum_v E_v \exp(-E_v/k_B T_v)}{\sum_v \exp(-E_v/k_B T_v)} \quad (8)$$

where E_v and N_v denote respectively the energy and density of the vibrational level v and k_B is the Boltzmann constant. In this equation, the vibrational temperature T_v is defined as the temperature for which the average energy of the non-equilibrium vibrational distribution function (VDF) equals the one of a Boltzmann equilibrium VDF.

Under non-equilibrium conditions, as we are considering in this section, the vibrational temperature T_v (regardless its definition) may be different from the translational gas temperature T_g. The usual procedure to self-consistently determine T_g in a discharge produced in a cylindrical tube [128] consists in solving the time-dependent gas thermal balance equation under isobaric conditions, considering that heat conduction is the main cooling mechanism:

$$n_m \frac{\partial T_g}{\partial t} = Q_{in} - \frac{8\lambda_g(T_g - T_w)}{R^2}. \quad (9)$$
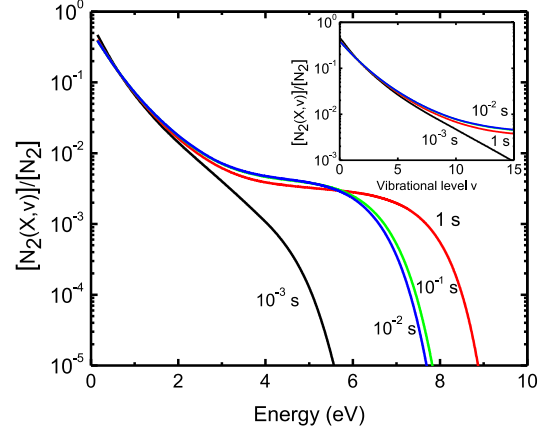

Fig. 15 Temporal evolution of the vibrational distribution function $[N_2(X,v)]/[N_2]$ in a DC discharge with 50 mA and a pressure of 7.5 Torr.

In this equation, T_g is the radially averaged gas temperature, assumed to have a parabolic profile across the discharge tube with radius R, n_m is the molar density, c_p is the molar heat capacity at constant pressure, Q_{in} represents the mean input power transferred to the translational mode (gas heating) per unit volume from different volume and wall processes, while λ_g denotes the thermal conductivity and T_w is the temperature at the wall. In molecular plasmas, the term Q_{in} must contain a wide range of different processes, including elastic collisions of electrons, non-resonant V-V collisions, V-T energy exchanges, exothermic chemical reactions [81, 96], as well as diffusion of electronically excited species, and recombination of atoms at the wall.

Figures 15, 16 report the time-dependent variation of the vibrational distribution function $[N_2(X,v)]/[N_2]$ in discharge and afterglow, while figures 17 and 18 show the corresponding *vibrational temperatures* computed from the different definitions described above, as well as the gas temperature, obtained from equation (9). The energy-representative vibrational temperature defined in equation (8) is computed iteratively from calculated values of E_v and N_v until the difference between the left and right-hand side of this equation is less than 0.1%. These modelling results have been obtained for the experimental conditions concerning a DC discharge with a current of 50 mA and subsequent afterglow produced at a pressure of 7.5 Torr in a cylindrical tube with an inner radius of 0.6 cm [129].

Figure 17 shows that the vibrational temperatures determined using different definitions are larger than the gas temperature, characterizing the degree of non-equilibrium of the VDF. This figure also shows that the vibrational temperatures determined from the first two and four vibrational levels (where the VDF exhibits a
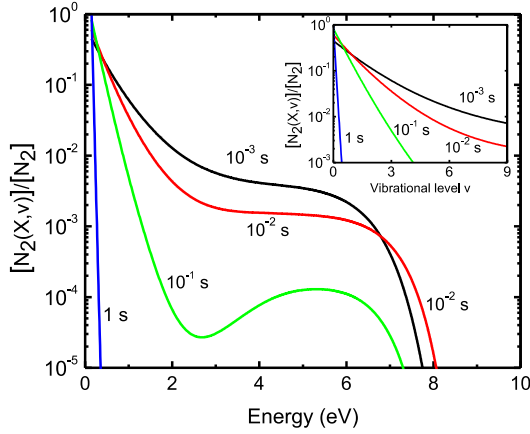
Fig. 16 Temporal relaxation of the vibrational distribution function $[N_2(X,v)]/[N_2]$ in the afterglow of DC discharge with 50 mA and a pressure of 7.5 Torr.
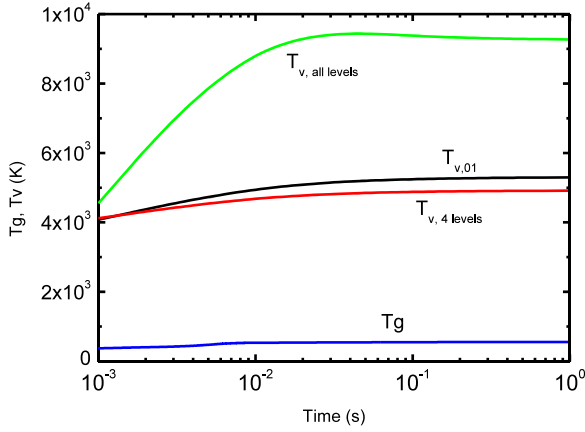

Fig. 17 Temporal evolution of the vibrational temperature of $N_2(X,v)$ in a DC discharge with 50 mA and a pressure of 7.5 Torr, considering the first two vibrational levels (black curve), the first four vibrational levels (red curve) and all vibrational levels (green curve). Predicted values for the gas temperature (blue curve) are also plotted.

similar slope - see inset of figures 15,16) are comparable. Moreover, these values are both lower than the one determined when all vibrational levels are considered, due to their dependence on the plateau and tail of the VDF. Figure 18, concerning post-discharge conditions, shows a similar behaviour in the beginning of the post-discharge. For longer afterglow times ($t > 0.1$ s) T_v has similar values independently of the way it is determined. This result is a consequence of the relaxation of the VDF shown in figure 16. Figure 18 also indicates that for these longer afterglow times, T_v starts to converge to the vaule of T_g.
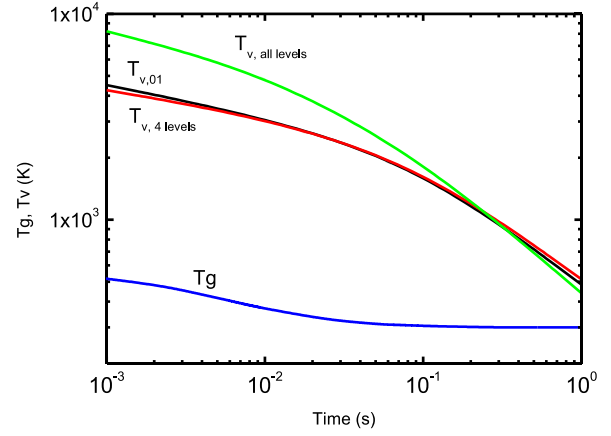

Fig. 18 Same as in figure 17, but for the subsequent afterglow.

4 Modelling Dielectric Barrier Discharges

The fundamental aspects described in the previous section, are usually investigated in 0D models considering the time evolution in the plasma bulk. However, cold plasmas in many real-world applications are markedly inhomegeneous. In these cases, as discussed in section 2, the physical effects due to the charge transport and its coupling with the electric field become relevant. Consequently, modelling the spatial profile of the plasma properties is of paramount importance. This is the case of the Dielectric Barrier Discharge (DBD).

Originally developed and employed for ozone generation [130], the DBD shares many features with the corona discharge, although the latter term is preferred for discharges between bare metal electrodes without dielectric. In a DBD device, indeed, either one or both the electrodes are covered with a dielectric layer. This has the effect of limiting the electric current and preventing spark formation [131].

One of the fundamental challenges in modelling the plasma physics taking place in a DBD is to adequately represent the non-equilibrium regime. In particular, this kind of discharges are characterized by physical phenomena spanning over considerably wide temporal and spatial scales [132]. In this section a fluid model devoted to the numerical solution of the continuity equation for the charged species under the drift-diffusion approximation is presented. The adoption of a Finite Volume approach allows for a straightfoward generalization of the code to two or three dimensions, as well as to the simulation of geometries requiring non-structured computational grids.

The operator-splitting technique is employed to separate the integration of the fluxes from both the electrostatic problem solution and the kinetic source terms

integration. Two different approaches are described for the electron transport modelling. The electrons can indeed be included in the drift-diffusion approach, or assumed to instantaneously adapt to the local electrostatic field caused by external applied voltages and the motion of the (slower) heavy ions. In the second case, the electron spatial distribution is obtained from the Boltzmann relation, leading to a non-linear electrostatic formulation.

One of the main goals of the developed model is to address the physical effects produced by the surface charge accumulation onto the dielectric layers. Indeed the latter constitutes one of the most important processes regulating the overall behaviour of a DBD device [133, 134]. For this reason, the computed values of surface charge deposited on the dielectric layers of a symmetric DBD configuration will be discussed.

4.1 Physical model

A drift-diffusion model is generally constituted by a set of continuity equations for each relevant species, coupled with an electromagnetic formulation of some kind, which is needed to determine the forces acting on the electrically charged species.

4.1.1 Drift-diffusion equation

In a ionized gas constituted by a mixture of S species, the number density n_s of the generic species s is governed by the equation:

$$\frac{\partial n_s}{\partial t} + \boldsymbol{\nabla} \cdot \boldsymbol{\Gamma}_s = \Omega_s, \tag{10}$$

where $\boldsymbol{\Gamma}_s$ is the $s-$th species flux. The the source term Ω_s at the right-hand side of Eq. 10 represents the species rate of change due to the elementary processes in the plasma (i.e., thermal ionizations, recombinations, attachments). The $\boldsymbol{\Gamma}_s$ flux of a charged species is determined by two driving mechanisms, i.e., the diffusion due to the number density gradient and the drift, which represents the collective motion of the charges due to the action of the electric field $\mathbf{E}$:

$$\boldsymbol{\Gamma}_s = -D_s \boldsymbol{\nabla} n_s + \text{sign}(q_s)\, n_s \mu_s \mathbf{E}, \tag{11}$$

where μ_s and D_s are the mobility and diffusivity of the considered species s, respectively.

It is worth noting that the $\mu_s \mathbf{E}$ represents the species drift velocity due to the electric field. Thus, Eq. 10 can be regarded ad a special case of advection-diffusion equation, in which the advective term is constituted by the drift. The flux definition in Eq. 11 can be extended to include cases where the advective transport takes place also due to a mass velocity $\mathbf{u}$:

$$\boldsymbol{\Gamma}_s = -D_s \boldsymbol{\nabla} n_s + n_s \mu_s \mathbf{E} + n_s \mathbf{u}. \tag{12}$$

In these cases, the model has to include an adequate fluid dynamic description, which may constitute an especially challenging task when the discharge is capable of affecting the flow field.

4.1.2 Plasma-dielectric interface

The interaction between the plasma and the dielectric walls plays a fundamental role in the discharge. Ions incident on the dielectric walls cause electron secondary emissions that constitute a significant contribution to the discharge dynamics. Furthermore, the charge deposition occurring on the wall can dramatically modify the applied electric field in the discharge region. A flux $\boldsymbol{\Gamma}_s$ of positive ions incident on the dielectric surface is assumed to produce $\gamma \boldsymbol{\Gamma}_s$ electrons per unit time and unit surface. A secondary emission event is assumed to leave a hole (i.e., a positive charge) on the dielectric surface. As a result, the rate of change of the surface charge density ρ_Σ on the dielectric wall is described by:

$$\frac{d\rho_\Sigma}{dt} = e\,\gamma \left(\sum_{s \in S_+} n_s \mu_s \right) E_n, \quad E_n > 0, \tag{13}$$

where S_+ is the set of positive ions.

Conversely, an electron flux $\boldsymbol{\Gamma}_e$ toward the dielectric wall is assumed to produce an instantaneous neutralization of holes, if they are present, or a negative charge accumulation otherwise. In both cases:

$$\frac{d\rho_\Sigma}{dt} = e\,\mu_e n_e\, E_n, \quad E_n < 0. \tag{14}$$

In Eqs 13,14, the normal unit vector is assumed to point outward from the discharge region. That is, the positive direction of the normal electric field points, E_n, toward the dielectric wall.

4.1.3 Electrostatics

The general assumption behind the electromagnetic formulation is that the electric current in the discharge is not strong enough to produce a relevant magnetic field. As a result, the electric field can be assumed to be conservative. Consequently, it can be expressed as the gradient of an electric scalar potential:

$$\mathbf{E} = -\boldsymbol{\nabla}\varphi. \tag{15}$$

Then, assuming linear, homogeneous and isotropic materials, the scalar potential is governed by the Poisson's equation:

$$\epsilon_0 \boldsymbol{\nabla} \cdot (\epsilon_r \boldsymbol{\nabla} \varphi) = -\rho, \tag{16}$$

where ϵ_0 and ϵ_r are the vacuum permittivity and the material relative permittivity, respectively. In the discharge region, the relative permittivity is assumed to be unitary ($\epsilon_r = 1$) and the charge density is determined by the distribution of the electrically charged species:

$$\rho = \sum_{s=1}^{S} q_s n_s. \tag{17}$$

A non-linear formulation of Eq. 16 can be obtained assuming that the electrons, being much faster than ions, instantaneously adapt to the local value of the electric potential, according to the Boltzmann relation:

$$n_e = n_{e,0} \, \exp\left[\frac{e(\varphi - \varphi_0)}{k_B T_e}\right], \tag{18}$$

where T_e the electron temperature in K, $n_{e,0}$ and φ_0 are the reference electron density and potential, respectively (i.e., $n_e(\varphi = \varphi_0) = n_{e,0}$). Introducing Eq. 18 and Eq. 17 in Eq. 16, one obtains:

$$\epsilon_0 \nabla^2 \varphi = -\left\{ \sum_{s \in S_H} q_s n_s - n_{e,0} \, \exp\left[\frac{e(\varphi - \varphi_0)}{k_B T_e}\right] \right\}. \tag{19}$$

where S_H is the set of heavy species. Equation 19 does not guarantee that the total electric charge in the considered domain V is equal to zero for arbitrary values of $n_{e,0}$ and ϕ_0. Indeed, these two parameters have to be chosen so that the total negative electric charge due to free electrons neutralizes the positive charge due to free ions and to the surface charge density that has been deposited on the dielectric surface S_d. Thus an additional constraint is added, to ensure the total charge neutrality:

$$\int_V \left\{ \sum_{s \in S_H} q_s n_s - n_{e,0} \, \exp\left[\frac{e(\varphi - \varphi_0)}{k_B T_e}\right] \right\} \mathrm{d}V +$$
$$+ \int_{S_D} \rho_\Sigma \mathrm{d}S = 0. \tag{20}$$

4.2 Numerical model

The problem formulated in the previous section has been numerically solved using a two dimensional Finite Volume (FV) approach. A discretization of the physical domain is performed through a subdivision in cells. For the sake of simplicity, a structured rectangular mesh will be assumed here onwards, although the method can be easily generalized to more complex mesh topologies.

4.2.1 2D drift-diffusion model

The drift diffusion equation for the s species is discretized at the point i by integrating Eq. 10 over the control volume ΔV_i, schematically represented in Fig. 19, and performing then the time integration by means of an explicit Euler scheme. Starting from the generic time instant t_k, the solution at t_{k+1} is determined by:

$$n_{s,i}^{(k+1)} = n_{s,i}^{(k)} - \frac{\Delta t}{\Delta V_i} \sum_{e \in \partial(\Delta V_i)} F_{s,e}^{(k)} + \Delta n_{s,i}^{(k)}, \tag{21}$$

where $F_{s,e}^{(k)}$ is the number of particles s leaving the cell i per unit time through the cell interface e with a ΔS_e cross section:

$$F_{s,e}^{(k)} = \Gamma_{s,n}^{(k)} \Delta S_e;$$

$\Delta n_{s,i}^{(k)}$ is the number density variation at node i of the species s during the time step Δt due to the source term $\Omega_{s,i}^{(k)}$. The normal flux component $\Gamma_{s,n} = \boldsymbol{\Gamma}_s \cdot \hat{\mathbf{n}}$ of the s species through the generic interface surface S_e, being the normal unit vector $\hat{\mathbf{n}}$ directed outward the control volume ΔV, can be split into a diffusive and a drift contributions. The diffusive flux can be discretized by means of a centred difference formula, while the drift component can be expressed by means of a first order upwind scheme. Referring to the interface between the nodes i and j, separated by a distance Δ_e (see Fig. 20), the normal flux can be expressed as:

$$\Gamma_{s,n} = C_{s,+} n_{s,i} + C_{s,-} n_{s,j}, \tag{22}$$

where, defining $E_n = \mathbf{E} \cdot \hat{\mathbf{n}}$ as the electric field normal component to the considered interface, and:

$$\begin{cases} v_{s,+} = \max\left[0, \mathrm{sign}(q_s)\mu_s E_{n,i}\right]; & \text{(23a)} \\ v_{s,-} = \min\left[0, \mathrm{sign}(q_s)\mu_s E_{n,E}\right]; & \text{(23b)} \end{cases}$$

the two $C_{s,+}$ and $C_{s,-}$ coefficients are defined as:

$$\begin{cases} C_{s,+} = \dfrac{D_s}{\Delta_e} + v_{s,+}; & \text{(24a)} \\ C_{s,-} = -\dfrac{D_s}{\Delta_e} + v_{s,-}. & \text{(24b)} \end{cases}$$

A higher accuracy in the evaluation of the normal flux component $\Gamma_{s,edge}$ can be achieved by means of an exponential fitting scheme [135–137]. Using a centred finite difference formula, the normal electric field at the
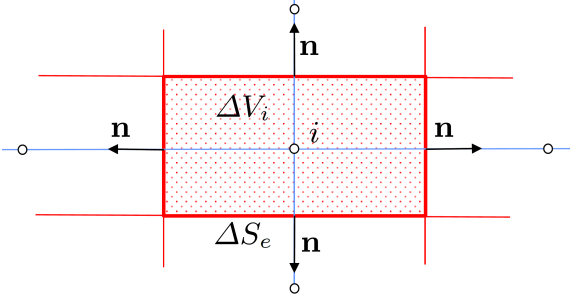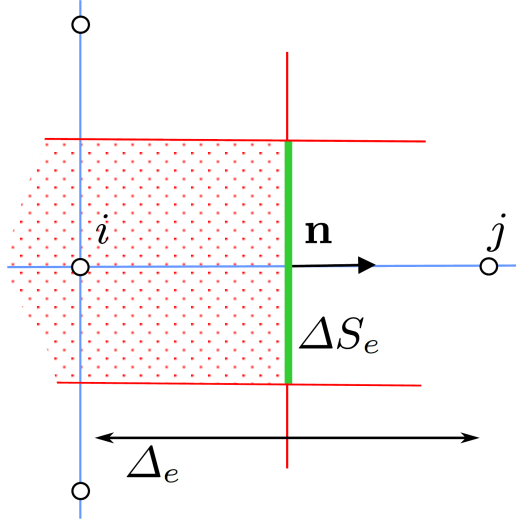
Fig. 19 Generic node centred volume

Fig. 20 Interface between two mesh nodes

interface can be expressed with a second order accuracy:

$$E_n = \frac{\varphi_i - \varphi_j}{\Delta_e}. \tag{25}$$

Then, the normal drift velocity $v_{s,n} = \text{sign}(q_s)\,\mu_s E_n$ of the considered species at the interface becomes:

$$v_{s,n} = \text{sign}(q_s)\,\mu_s \frac{\varphi_i - \varphi_j}{\Delta_e}. \tag{26}$$

Defining:

$$\alpha_s = \frac{v_{s,n}\,\Delta_e}{D_s} = \text{sign}(q_s)\,\frac{\mu_s}{D_s}\,(\varphi_i - \varphi_j)\,, \tag{27}$$

the numerical flux at the interface can be expressed using Eq. 22 using the following expressions for the $C_{s,+}$ and $C_{s,-}$ coefficients:

$$\begin{cases} C_{s,+} = v_{s,n} \dfrac{\exp(\alpha_s/2)}{\exp(\alpha_s/2) - \exp(-\alpha_s/2)}; & (28a) \\[2mm] C_{s,-} = v_{s,n} \dfrac{\exp(-\alpha_s/2)}{\exp(\alpha_s/2) - \exp(-\alpha_s/2)}. & (28b) \end{cases}$$

It is worth noting the close relation between the α_s coefficient defined in Eq. 27 and the local Peclet number $\text{Pe}_{s,\Delta}$ for the given advection-diffusion problem, being:

$$\text{Pe}_{s,\Delta} = |\alpha_s| = \frac{\mu_s}{D_s}\,|\varphi_i - \varphi_j| \tag{29}$$

A more convenient form of the above coefficients is obtained by distinguishing the two cases in which the species drift velocity is positive and negative: for $v_{s,n} > 0$

$$\begin{cases} C_{s,+} = v_{s,n} \dfrac{1}{1 - \exp(-\text{Pe}_{s,\Delta})}; & (30a) \\[2mm] C_{s,-} = v_{s,n} \dfrac{\exp(-\text{Pe}_{s,\Delta})}{1 - \exp(1 - \text{Pe}_{s,\Delta})}; & (30b) \end{cases}$$

for $v_{s,n} < 0$

$$\begin{cases} C_{s,+} = v_{s,n} \dfrac{\exp(-\text{Pe}_{s,\Delta})}{\exp(-\text{Pe}_{s,\Delta}) - 1}; & (31a) \\[2mm] C_{s,-} = v_{s,n} \dfrac{1}{\exp(-\text{Pe}_{s,\Delta}) - 1}; & (31b) \end{cases}$$

The expressions for computing the $C_{s,-}$ and $C_{s,+}$ coefficients tends to an indeterminate form $0/0$ when the drift velocity $v_{s,n}$ tends to 0. To avoid this, when $\text{Pe}_{s,\Delta} < \tau$, where τ is a user specified threshold, the numerical flux can be evaluated as

$$\Gamma_{s,edge} = D_s \frac{n_{s,i} - n_{s,est}}{\Delta_e} + v_{s,n} \frac{n_{s,i} + n_{s,est}}{2}, \tag{32}$$

The $C_{s,-}$ and $C_{s,+}$ coefficients in the above expression become:

$$\begin{cases} C_{s,+} = \dfrac{D_s}{\Delta_e} + \dfrac{v_{s,n}}{2} & (33a) \\[2mm] C_{s,-} = -\dfrac{D_s}{\Delta_e} + \dfrac{v_{s,n}}{2} & (33b) \end{cases}$$

At the interfaces between the plasma and the dielectric walls, a flux of a generic species can produce a number of possible events, as described in Sect. 4.1.2. In this work, the flux toward the wall of a species s is evaluated as the sum of a drift contribution and a term due to the thermal velocity v_{th}:

$$\Gamma_{s,wall} = [\text{sign}(q_s)\mu_s E_n + v_{s,th}]\,n_s, \tag{34}$$

with

$$v_{s,th} = \frac{1}{4}\sqrt{\frac{3\,k_B\,T_s}{m_s}}.$$

Recombinations and depositions caused by a flux of the species s toward the wall are considered in Eq. 21 as fluxes leaving the cell. A flux $\Gamma_{+,wall}$ of positive ions

incident to the dielectric surface causes the wall to produce an electron flux $\Gamma_{e,wall}$ due to secondary emission:

$$\Gamma_{e,wall} = -\gamma \Gamma_{+,wall}, \tag{35}$$

which is considered in Eq. 21 for the electrons as a flux entering the cell. The Courant-Friedrichs-Lewy (CFL) condition impose an upper bound to the time step Δt in order to guarantee the stability of the numerical scheme Eq. 21:

$$\Delta t < \min \left[\frac{1}{|\mu_s E/min(\Delta| + |D_s/(2\Delta^2)|} \right] \tag{36}$$

with:

$$\Delta = \min \left(\Delta_e \right)$$

4.2.2 2D electrostatic model

Electrostatics is numerically solved discretizing Eq. 16 by means of a finite volume scheme. Referring to Fig. 19, the discrete equation for a generic cell i internal to the calculation domain can be written as:

$$\sum_{e \in \partial(\Delta V_i)} F_{D,e} = Q_i, \tag{37}$$

where $F_{D,e}$ is the electric displacement flux at the interface e:

$$F_{D,e} = \epsilon_0 \frac{\varphi_i - \varphi_j}{\Delta_e} \Delta S_e, \tag{38}$$

and Q_i is the total electric charge in the cell:

$$Q_i = \sum_{s=1}^{S} q_s n_s \, \Delta V. \tag{39}$$

Boundary nodes are dealt with utilizing the cell scheme represented in Fig. 21. We consider a δ_d thick dielectric whith a relative permittivity $\epsilon_{d,r}$ interposed between the discharge and the electrode, which is set to an applied voltage $\varphi_{ext}(t)$. The electric displacement flux through the interface between the boundary node and the electrode is:

$$\Phi_{D,wall} = \epsilon_0 \epsilon_{d,r} \frac{\varphi_i - \varphi_{ext}(t)}{\delta_d} \Delta S_{i,electrode}. \tag{40}$$

Conversely, the electric displacement flux through the interface between two adjacent boundary nodes i and j is:

$$\Phi_{D,ij} = \epsilon_0 \left(\frac{\varphi_i - \varphi_j}{\Delta_{i,k}} \right) \left(\Delta S'_{i,k} + \epsilon_{d,r} \Delta S''_{i,k} \right). \tag{41}$$
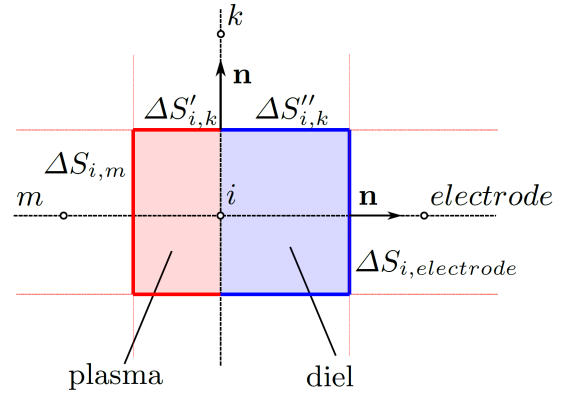

Fig. 21 Control volume shared between plasma and dielectric

In computing the total electric charge in a boundary cell, the surface charge density has to be taken into account:

$$Q_i = \sum_{s=1}^{S} q_s n_s \, \Delta V + \rho_{\Sigma,i} \, \Delta S_{wall}. \tag{42}$$

By applying the discrete equation 37 to all the nodes, an algebraic system is obtained:

$$[K] = \{RHS \left(n_1, n_2, ..., n_S \right)\} . \tag{43}$$

If all the species are tracked individually, considering the drift-diffusion equation for each of them, the linear algebraic system resulting from the discretization of electrostatics has to be solved at each time step, recalculating the right hand side term to account for the changes in the distributions of the species number densities. In this case, the stability condition Eq. 36 would imply an upper bound to the time step based on the species with the higher mobility, i.e., electrons. This limitation can however be mitigated using the Boltzmann relation to evaluate the equilibrium electron density number density, and solving the resulting non linear Poisson's equation 19. In this case, the discretization problem yields a non linear system, where the right hand side term depends on the number density of the heavy particles, on the electric potential and on the reference potential φ_0

$$[K] = \{RHS \left(n_1, n_2, ..., n_S, \varphi, \varphi_0 \right)\} . \tag{44}$$

For a given value of φ_0, a Newton-Raphson iterative scheme is used to solve the non linear system Eq. 44. As noted in 4.1.3, the reference potential φ_0 has to be adjusted to meet the global charge neutrality condition Eq. 20. This is done using a bisector method running externally to the Newton-Raphson solver.
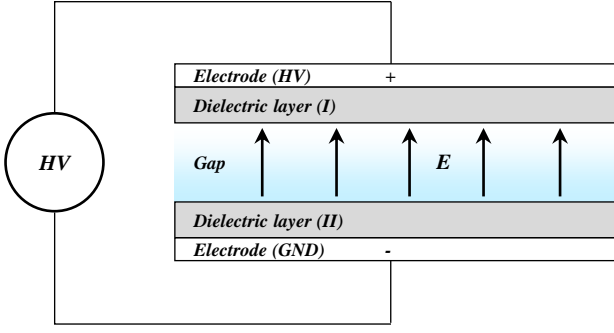
Fig. 22 Schematic representation of the modeled DBD reactor volumetric reactor

Table 1 Electrical mobility coefficients for ions and electrons in dry air, from [138]. N is the background neutrals density [m^{-3}], T the heavy ions temperature [K] and T_e the electron temperature [K]

Species	Mobility [m V^{-2} s^{-1}]
N$_2{}^+$ [139]	$\frac{1}{N}\min\left(0.84 \times 10^{23}T^{-0.5}, 2.35 \times 10^{12}\left(\frac{E}{N}\right)^{-0.5}\right)$
O$_2{}^+$ [139]	$\frac{1}{N}\min\left(0.75 \times 10^{23}T^{-0.5}, 2.03 \times 10^{12}\left(\frac{E}{N}\right)^{-0.5}\right)$
O$_2{}^-$ [140]	$\frac{1}{N}\min\left(1.18 \times 10^{23}T^{-1/2}, 3.61 \times 10^{12}\left(\frac{E}{N}\right)^{-0.5}\right)$
e$^-$ [141]	$\frac{1}{N}3.74 \times 10^{19}\exp\left(33.5\ln(T_e)^{-0.5}\right)$

4.2.3 Source terms

At the k-th time step, a semi implicit approach was adopted to compute the array $\{\Delta N_i\}_\Omega^{(k)}$, whose generic entry $\Delta N_{s,i}^{(k)}$ has been defined above in Eq. 21. Let's define $[O_i^{(k)}]$ as the local Jacobian matrix of the source terms at point i. The generic term $o_{s,w}^{(k)}$ in $[O_i^{(k)}]$ is defined as the derivative of the source term $\Omega_{s,i}^{(k)}$ of the species s at the point i, with respect to the number density $n_{w,i}^{(k)}$, referred to the species w at the point i. The source term array can be now linearised in the form $\{\Omega_i\}^{(k+1/2)} = \{\Omega_i\}^{(k)} + [O^{(k)}(i,j)]\Delta t/2$. The increment array $\{\Delta N_i\}_\Omega^{(k)}$ in the Δt time interval due the the chemical reactions is found by solving the system:

$$[M]\{\Delta N_i\}_\Omega^{(k)} = \{\Omega_i\}^{(k)}\Delta t, \tag{45}$$

where:

$$[M] = [I] - \frac{1}{2}[O_i^{(k)}]\Delta t.$$

4.3 Simulation of a DBD volumetric reactor

In this section, a DBD volumetric reactor is modelled using the developed methodology. The modelled device – shown in Fig. 22 – is symmetric, with both high voltage (HV) and ground (GND) electrodes constituted by a 1 cm^2 square thin copper plate, covered by a 0.2 mm thick Kapton dielectric layer. The gap is filled with atmospheric pressure air, and has a thickness of 0.4 mm. The configuration is assumed to be powered by a 4.8 kV sinusoidal voltage, operated at a frequency of 15 kHz. The temperature of all ionic species is set to 400 K, while the electron temperature is assumed to be 2 eV.

4.3.1 Considered species

The heavy species accounted for in the drift-diffusion model are N$_2{}^+$, O$_2{}^+$ and O$_2{}^-$. The electrical mobility of the above species and electrons is computed using the expressions in [138], reported in Table 1 (along with their original reference) for the reader's convenience. The quantity N in the expressions represents the background neutrals density, expressed in m^{-3} while T and T_e are the ionic and electronic temperatures in Kelvin, respectively.

Once the mobility coefficient is obtained with the above described procedure, the diffusion coefficient is derived from the Einstein relation:

$$\frac{D_s}{\mu_s} = \frac{k_B T_s}{|q_s|}. \tag{46}$$

The developed numerical code implements a simple kinetic model in [138], consisting of slight modifications of rate coefficients from [142]. The time-integration of the chemical kinetics source terms, i.e., the right-hand side of Eq. 10, is performed with the semi-implicit numerical scheme described in [143].

4.3.2 Domain discretization

A two-dimensional 0.2 mm x 1 cm x-y plane domain has been considered, being the x direction normal to the dielectric walls. It is worth noting that the model described in this work can easily be represented in r-z domains, which are more appropriate for devices with axial symmetry geometries. Despite having used a 2D model, results exhibit a very weak dependence on the y variable (i.e., the direction pointing parallel to the surface of the dielectric), and the problem is virtually a one-dimensional problem. The results discussed in this section are referred to the DBD reactor center line.

Given that an explicit approach has been used to to time-integrate Eq. 10, the employed Δt is subjected to the stability condition defined in Eq. 36. Hence, the code performances are strongly dependent on both the minimum grid spacing and number of employed grid nodes. The minimum employed grid spacing is subjected to the requirement of resolving the Debye length, which in turn depends on the electron number density and temperature. The highest values of electron number density are usually found at the edges of the domain, where the different species tend to accumulate as a consequence of the drift induced by the externally applied electric field. For this reason a regular non-uniform grid has been employed, in which the grid spacing is specified by defining the ratio $k_{s,x}$ between the length associated with the given cell Δx_k and the following one, Δx_{k+1}. In this way, $k_{s,x}$ is defined by:

$$k_{s,x} = \frac{\Delta x_{k+1}}{\Delta x_k}. \tag{47}$$

The described procedure represents a simpler alternative to more sophisticated approaches based on adaptive mesh refinement (AMR), where the spatial distribution of the grid nodes is dynamically adapted to increase the grid density where the physical properties change sharply and vice versa [144]. In the field of DBD modelling, different variations of this technique have led to performance improvements in several works employing both structured [145, 146] and non-structured meshes [2, 147].

4.3.3 Simulation results

The described computational code has been employed to simulate the main plasma dynamics taking place during two cycles of the externally applied voltage (V_{ext}). Figure 23 shows the externally applied voltage (V_{ext}), along with the computed electric potential difference over the gap during the simulation (V_{gap}). As can be observed, the DBD transient behaviour is mainly limited to the first half wave, and the results shown in the second wave can be considered as representative of the periodic steady-state solution.

With reference to Fig. 22, V_{ext} is enforced between the two electrodes, marked respectively as HV and GND. V_{gap} is computed as the difference between the electric potential (yielded by the solution of the Poisson's equation) on the first and last nodes of the grid. Hence, if the nodes are numbered from 1 to n, the gap voltage is defined as:
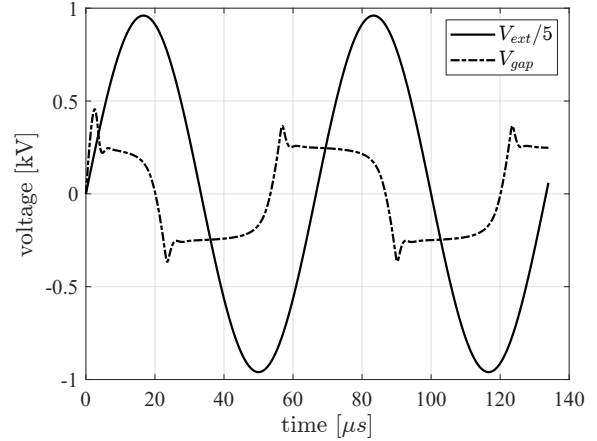
$$V_{gap} = \varphi_1 - \varphi_n. \tag{48}$$

Fig. 23 Electric potential difference over the gap (V_{gap}) during the first two cycles of the externally applied voltage (V_{ext}), multiplied by a scale factor of 1/5 for the sake of readability

From a physical standpoint, $\Delta\varphi_{gap}$ represents the voltage to which the air gap is effectively subjected. This is in general different from the externally applied voltage, because of three distinct physical mechanisms:

1. Each dielectric layer causes a voltage drop, determined by its thickness and relative permittivity ($\epsilon_{r,d}$);
2. The charged species in the gap are free charges, subjected to drift caused by the presence of external electric fields. The local electric field generated by such volumetric charge densities opposes the external field;
3. Analogously to the physical role played by free charges in the gap, the (bound) charges accumulated in the dielectric layers also contribute to screen the gap from the electric field generated by the high-voltage source.

In Fig. 23, the combination of the three listed mechanisms causes V_{gap} to reach a maximum value of 454 V during the first quarter of the (first) cycle, after 2.4 µs from the beginning of the simulation. Then, while V_{ext} continues to increase, V_{gap} starts to progressively decrease, reaching a null value in the second quarter. During the first half of the cycle, a positive voltage is enforced on the HV electrode, adjacent to dielectric layer I. An electric field is consequently generated in the gap, causing the negative charges (negative ions and free electrons) to drift towards the anode (the HV electrode). Similarly, the positive ions are pushed towards the GND electrode, which acts as the cathode. Hence, the two dielectric layers I and II are subjected to a flux of negative and positive charges, respectively.

The surface charge accumulated in the dielectric layers during the considered two cycles of the external waveform is depicted in Fig. 24. As one can see by comparing Figs. 23 and 24, both dielectrics start to ac-
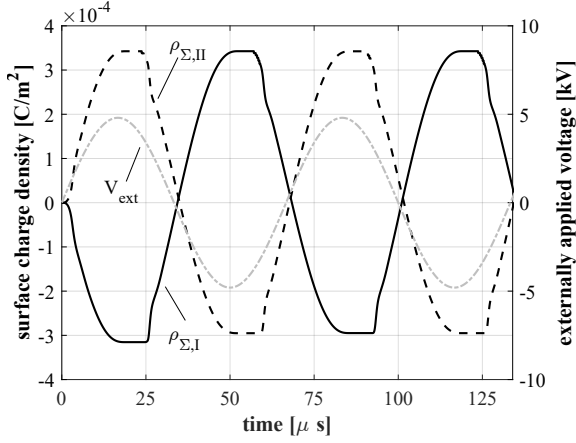
Fig. 24 Surface charge density deposited onto dielectric layers I and II (see Fig. 22), over two cycles of the externally applied voltage (V_{ext}).
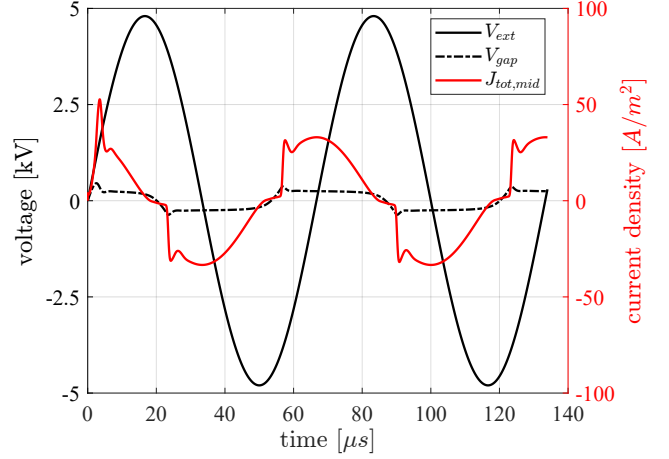

Fig. 25 Total current density (J) computed at the midpoint of the gap during the first two cycles of the performed simulation, plotted against the externally applied voltage (V_{ext}) and the electric potential difference applied to the gap (V_{gap})

cumulate charges (of opposite sign) as soon as a voltage is applied to the reactor. With reference to Fig. 24, the first *charging front* ends at 16.8 µs, when the external voltage reaches its maximum value. At this point, as can be verified in Fig. 23, the external voltage has been almost completely screened out by the surface charge. The reversal of the gap voltage during the second quarter of the external voltage (after 20 µs) is caused by the surface charge, which retains its (maximum) value when V_{ext} starts to decrease after its peak at 16.8 µs.

The results shown in Fig 24 have been obtained by assuming that the charge accumulation process is only caused by drift and diffusion fluxes. However, as previously discussed, incident fluxes due to the random motion associated with the thermal velocity of the species can also be responsible for the accumulation of surface charges on to the dielectric layers. The described simulation was then repeated including the effect of v_{th}, showing negligible qualitative differences with respect to the results in Fig. 24. Hence, at least for the conditions simulated in this present study, the electric field induced charge drift appears to be the dominant physical mechanism behind the surface charge accumulation process.

Figure 25 shows the computed current density in the midpoint of the gap during the performed simulation.

The current density, J, has been obtained as the sum of the conduction and displacement currents:

$$J = J_c + \frac{\partial D}{\partial t}. \tag{49}$$

In Eq. 49, the conduction current J_c is obtained summing the local fluxes of the charged species:

$$J_c = \sum_s^{N_s} q_s n_s u_s, \tag{50}$$

where N_s is the number of considered charged species, while n_s and u_s are the local number density and velocity of the given specie s.

For what concerns the displacement current term in Eq. 49, this is obtained from the electric field at a generic time instant k and the electric field at $k-1$, divided by the time interval $\Delta t_{k,k-1}$ between the two considered instants:

$$\left.\frac{\partial D}{\partial t}\right|^{(k)} = \epsilon_0 \frac{E^{(k)} - E^{(k-1)}}{\Delta t_{k,k-1}}. \tag{51}$$

Alternatively, the total current can also be computed using the total displacement current over one of the dielectric layers. Considering e.g. dielectric layer I, the total displacement current over I be obtained using Eq. 51, where the displacement vector is evaluated with the following expression:

$$D_I = \epsilon_0 \epsilon_{r,d} \frac{V_{ext} - \varphi_i}{d}, \tag{52}$$

where (using the notation of Fig. 22) φ_i is defined as the electric potential of the grid node adjacent to the dielectric layer, and d is the thickness of dielectric layer I.

Overall, the obtained values of current density are compatible with usual ranges typical of atmospheric pressure DBDs [148, 149]. As can be verified by comparing Fig. 25 with Fig. 23, the observed periodic positive and negative peaks of the computed current density

are located between the second and fourth quarters of each cycle of V_{ext}. Indeed, the highest current density $J_{tot,mid}$ values are obtained in correspondence of the gap voltage (V_{gap}) reversals, due to the combination of the external (decreasing) voltage (V_{ext}) and the electric field produced by the surface charge density accumulated on to the dielectric layers.

5 Discharge in contact with water

Among other applications , such as flow actuators, plasma-assisted combustion, DBDs are specifically used to activate water for biomedical purposes.

Discharges taking place directly within liquid media, in particular in water, have attracted increasing attention since half a century [150,151]. The presence of ionized channels within water triggers kinetic phenomena producing reactive species useful for inactivation of chemical and biological compounds. The breakdown mechanism in the liquid phase usually occurs for very intense electric fields, several times higher with respect atmospheric pressure air [152]. Electrohydraulic discharges are prone to thermalization and to avoid fast temperature increment, and limiting, on a parallel plane, treatment energy dose, high pulsated electric fields are usually utilized to ignite this typology of discharges [153]. The need to limit operating voltage, energy consumption and discharge temperature, led researchers to explore new ways to take advantage of water chemistry promoted by the presence of discharges. For these reasons, in the last two decades, studies dealing with discharges taking place in air and in contact with water have increased in an enormous way [154]. The plasma can be ignited in the gas phase, taking advantage of limited breakdown voltages, subsequently propagating onto the water surface. In these gas/water reactors, water usually acts as one of the electrodes. Two main categories of reactors exist: discharge over water surface and bubbling reactors. The former deals with discharges generated between an electrode close to the water, and the water surface itself [155–157]. These reactors can sustain different kinds of discharges, depending on the particular geometry and voltage waveform. Corona discharges [158,159], Dielectric Barrier Discharges (DBDs) [160,161] and gliding arcs [162,163] are most common plasma typologies utilized. On the other hand, bubbling reactors flush air bubbles within the water, and the plasma is ignited within these bubbles or onto the separation surface water-bubble [164,165]. This configuration usually enhances exchange surface between air and water, maximizing the amount of charges and reactive species diluted within the liquid.

When the discharge is ignited in the gaseous phase, air kinetic takes place. As far as humidity is always present, gas chemistry must also consider air-water interactions (at least water vapour). Main chemical products are usually ozone, nitrogen oxides, oxygen peroxide and peroxide radical [152]. These molecules are very strong oxidant species, able to interact with chemical compounds and biological substrates. These species produced within the gas phase, subsequently reach the liquid surface, being diluted with the water volume. Moreover, as far as the discharge is directly in contact with the water, free charges are directly produced and diluted within the water itself. The presence of highly reactive species and charged particles directly inside the water volume, triggers a complex set of secondary chemical reactions leading to the formation of nitrates, nitrites, peroxinitrates and increasing water acidity [166]. The water activated by the discharge becomes a powerful medium useful for both pollutant treatment [167,168] and for decontamination purposes against microorganisms [169].

The target sample can be directly suspended or diluted within the water and then treated by the discharge. In this manner, direct treatment is carried out. Another possible way is to treat the water, producing the so called Plasma Activated Water (PAW) or Plasma Enhanced Water (PEW) [170]. This water comprehensive of active species can be subsequently used, operating an indirect treatment on samples. PAW can thus be produced, stored, and subsequently utilized for decomposition or decontamination purposes. Storage temperature has a huge effect in PAW properties [171]. A temperature of about $-80\,°C$ must be utilized to keep the chemical changes induced by the plasma unaltered during long storage periods [172].

5.1 Air/water Dielectric Barrier Discharge for pathogen decontamination purposes: a case test

In this section, a DBD volumetric reactor used for the decontamination of Eimeria oocytes is physically, chemically, and biologically described. The aim of this case test is to show the complex set of diagnostics needed for an *all-round* characterization of both reactor and biological effectiveness.

5.1.1 Physical and chemical reactor characterization

Reactor geometry is displayed in Fig. 26. A 8 cm in diameter polystyrene Petri dish, filled with 20 mL of deionised water, is placed between the electrodes of a plane-to-plane volumetric DBD. The lower electrode is
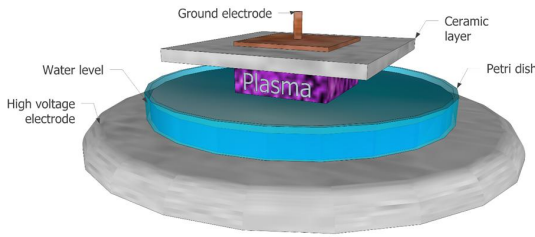
Fig. 26 DBD reactor discharge schematic

Fig. 27 Images of the discharge when supplied with the sinusoidal generator and exposure time = 210 μs (a) and when supplied with the nanosecond pulse generator and exposure time = 1 μs (b).

a stainless-steel plate connected to a high voltage generator. The upper electrode is a copper strip with an area of 3×3 cm^2, connected to ground terminal. A 3 mm thick 5×5 cm^2 ceramic slab covers the upper electrode surface. An atmospheric pressure air gap is left between the water surface and the dielectric layer. The reactor was supplied with a high frequency voltage with both a sinusoidal and a nanosecond-pulsed waveform. When the sinusoidal voltage source is used, a 3 mm air gap is set between ceramic layer and water surface. This is the smallest distance that avoids the formation of the Taylor cone, preventing water attachment onto the ceramic surface. Supplied peak voltage is fixed at 18 kV, 4.7 kHz, with a duty cycle of the 5%. This small duty cycle value allows to limit both discharge translational temperature and average power. When the reactor is supplied with the nanosecond-pulsed generator, the air gap is diminished up to 1 mm, because the applied voltage is characterized by very fast dynamics, strongly limiting the movement of water surface. Supplied voltage was set to 10 kV at 1 kHz, with rise time of about 10 ns. The chosen supplying conditions allow to obtain a comparable plasma power consumption when both power sources were used. A detailed description of the utilized setup is reported in the paper [173].

Discharge morphology is studied by utilizing a fast iCCD camera (Stanford Computer Optics 4 Picos model). Exposure time was set to 210 μs in order to visualize the time interval corresponding to one voltage period, when utilizing the sinusoidal power supply. For the nanosecond pulse generator, exposure time is set to 1 μs. Images of the whole discharge filling the air gap for both power supplies are depicted in Fig. 27.

Images clearly show that the discharge ignited by the sinusoidal generator presents a filamentary behaviour. On the contrary, when nanosecond power supply was used, a quite homogeneous glow-like discharge was produced. This different behaviour in discharge structure is related in the following, with different heavy particle temperatures measured for the two supplying conditions.

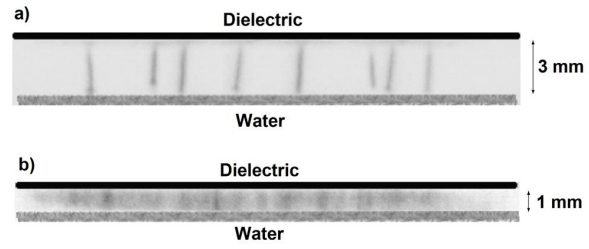Electron and translational temperatures were experimentally estimated by utilizing Optical Emission Spectroscopy (OES). Spectra were collected with a collimator lens (focal ratio f4, focal length 40 mm) focused on the discharge region. The signal is transferred through an optical fibre cable to a Jobin-Yvon HR-460 monochromator (focal ratio f5.3, focal length 460 mm) coupled with the iCCD Camera. The camera shutter is left open for 1 ms. OES setup collects most of the light during the discharge phase and coming from the core of the discharge itself. Temperatures derived from spectra must be thus interpreted as average values, without accounting for space and time distributions. Electron temperature T_e is derived from the ratio between the line intensities of the First Negative System (FNS) band head peak of N_2^+ at 391.4 nm and the Second Positive System (SPS) band head peak of N_2 at 394.3 nm [174]. This method applies when mentioned electronic states are assumed to be excited by electron impact collisions from the ground state. Moreover, a Maxwellian electron energy distribution function (eedf) is assumed. Under the experimental conditions investigated, the first assumption is quite valid due to the high-pressure condition [175]. The second assumption is not completely fulfilled as in DBD plasmas the eedf usually presents local departures from Maxwellian distribution especially during the afterglow phase [176]. Deviations in the afterglow are mainly caused by superelastic collisions between cold electrons and metastable state molecules. As far as the spectrum is mainly collected during the discharge phase, the assumption of a Maxwellian distribution for electron energies during this time interval may be attempted. This simplified assumption has been confirmed by plasma-kinetic simulations accounting for a self-consistent coupling of the state-to-state kinetics of the air mixture with the Boltzmann equation of free electron kinetics [177] and by utilizing Bolsig + accounting for superelastic collisions [178]. Measured and simulated temperatures are very similar in all conditions. Spectra reported in Fig. 28 have been utilized for the above-mentioned line ratio method.
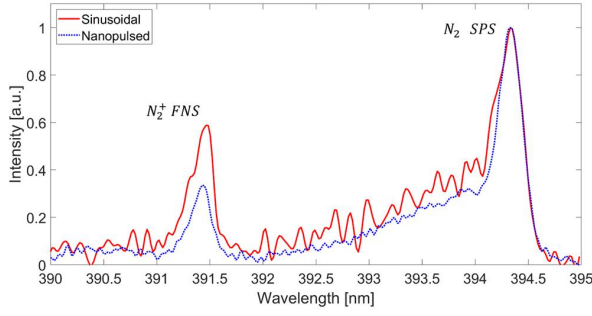
Fig. 28 Emitted spectra by the discharge supplied with the sinusoidal generator (red continuous line) and nanosecond pulse generator (blue dotted line).

Table 2 Rotational temperature (T_r) and measured electron temperature (T_e) for both sinusoidal and nanosecond-pulsed discharge

	T_r [K]	T_e [eV]
sinusoidal	475	2.6 ± 0.1
ns-pulsed	318	2.1 ± 0.1

Rotational temperatures of the excited electronic states of molecular nitrogen N_2 were determined by considering two spectral windows of 20 nm centred at 376 nm and 400 nm. They correspond to the transitions of the SPS of N_2, $C_3\Pi_u \rightarrow B_3\Pi_g$, with a variation of the vibrational number $\Delta\nu = 2$ and $\Delta\nu = 3$, respectively. The rotational temperature was obtained by comparing the measured spectra of the SPS with the synthetic ones simulated by means of the software SPECAIR [179]. In the calculations, the translational temperature was assumed to have the same value as the rotational one [180]. Bruggeman et al [181] showed that this approach is consistent and robust. They also demonstrated that, at the present conditions, the rotational temperature gives a good estimation of the gas temperature in the plasma region. Estimated temperatures are reported in Tab. 2. A higher value in the rotational temperature found when utilizing the sinusoidal generator, indicates that this discharge causes a higher heating effect on the gas than the nanosecond-pulsed one. This is partially related with the constricted regime observed in the sinusoidal discharge structure (see Fig. 27 a). Despite this relatively high temperature, water temperature increment has been found to be below 2.5 °C after 12 minutes treatment. This is due to the limited discharge filament volumes and duty cycle operation. When the nanosecond generator was utilized, an even more limited water temperature increment of 1.5 °C was found after 12 minutes treatment.

Chemical analysis of treated water has been carried out as well. Ozone concentration is measured by using the UV absorption method [182]. Hydrogen perox-
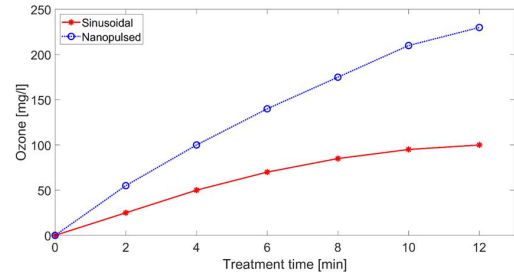

Fig. 29 Ozone concentration as a function of the treatment time when using sinusoidal generator (red continuous line) and nanosecond pulsed generator (blue dotted line)

Fig. 30 Hydrogen peroxide concentration as a function of the treatment time when using sinusoidal generator (red continuous line) and nanosecond pulsed generator (blue dotted line)
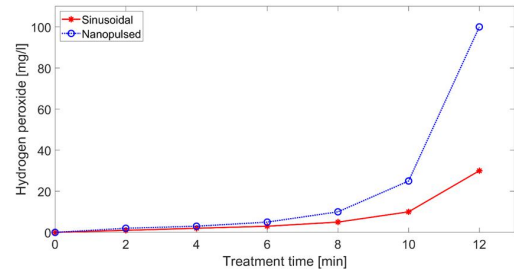
ide concentration is detected by using Macherey-Nagel QUANTOFIX Peroxide analytical strips. These methods and their applicability are reported in [173].

Ozone concentration as a function of treatment time measured within the water by using both power supplies is shown in Fig. 29. Ozone concentration increases for both supplying conditions. When sinusoidal generator is used, O_3 concentration is lower because of the higher translational temperature of the discharge, increasing the rates of ozone reactions leading to the formation of N_xO_y.

Hydrogen peroxide concentration is reported in Fig. 30. The figure clearly shows that higher concentration values are reached when utilizing nanosecond pulsed discharge. As a matter of fact, the production of H_2O_2 mainly occurs in the liquid due to the presence of hydrated electrons [183]. Their concentration strongly depends on the number of electrons produced in the plasma volume and reaching the water surface. The fast ionization front generated by the nanosecond pulsed power source, produces a plasma with a higher electron density, thus promoting the production of hydrogen peroxide into the liquid phase [173].
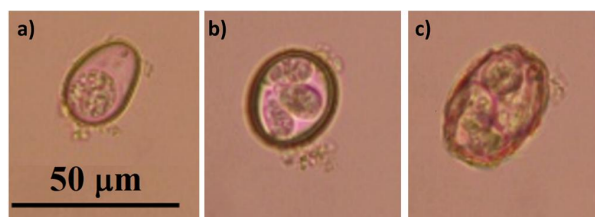
Fig. 31 *Eimeria* oocytes unsporulated (a), sporulated (b) and damaged (c)

Fig. 32 Damaged oocytes as a function of treatment time for sinusoidal (red continuous line) and nanosecond pulsed (blue dotted line) generators

5.1.2 Biological effectiveness of the DBD air/water reactor

The reactor described in the previous section was utilized to treat *Eimeria* oocytes immersed in water suspension. These coccidian types belong to *Toxoplasma gondii* and *Cryptosporidium parvum*, two of the most severe zoonotic agents worldwide [184]. These parasites demonstrated a strong resistance to usual chemical and physical compounds because of their outer shielding structure. Coccidia were collected in poultry farms with clinical coccidiosis evidence, and subsequently suspended in a water solution (coccidia preparation is described in reference [185]). The contaminated liquid was exposed to the plasma for 4, 8 and 12 minutes and one control sample was prepared for each of the two considered excitation voltage waveforms. The treated suspensions were diluted with an equal volume of a 2.5% potassium dichromate solution ($K_2Cr_2O_7$) and then transferred in sporulation chambers to obtain the infectivity stage. After the incubation, a hundred of oocytes were extracted and they were analysed with optical microscope to detect their sporulation stage. In Fig. 31 unsporulated (a), sporulated (b) and damaged (c) stages are displayed. Non-infectous oocytes are unsporulated and damaged oocytes (a and c).

Plasma treated water is particularly effective in the increment of damaged oocytes. For both supplying conditions, after a treatment time of 4 minutes, the number of damaged oocytes was about doubled. By increasing the treatment time, incremental plasma action was less effective (Fig. 32). The efficiency of plasma treatment in damaging oocytes is of particular relevance because of the ir three-wall structure make these parasites to strongly resist to common chemical and physical compounds used for disinfection.

6 Microwave plasma for diamond growth: application to jewelry.

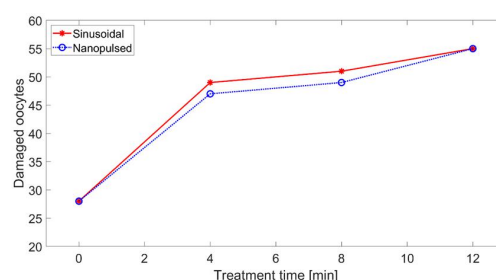Besides DBDs, microwave (MW) discharges constitute another efficient source to sustain a plasma in high-pressure conditions. An interesting and fancy application of these plasma sources involves the deposition of diamond films and the growth of diamond crystals.

Diamond, as an exceptional material can be used for many applications in particular those that need extreme properties. We can note in particular some edge applications such as quantum information using diamond NV-centers as well as power electronics that need very high crystalline quality [186–188]. Here, we will concentrate on another edge application that is today in huge development, i.e. diamond for jewelry. This application, on the opposite to the other s, needs very thick diamond layer (> 4 mm) in order to make cut diamonds from 0.5 to 3 carats or even more, and a fine control of impurities.

Growing diamond in a plasma is based on the fact that instead of HPHT (High Temperature High Pressure) process that occurs, as growth in mines, in the thermodynamic stability of carbon, plasma growth is driven by a kinetics-controlled process [189–193]. As a matter of fact, condensation processes of both graphite and diamond and etching processes of both graphite and diamond are occurring simultaneously. The balance of these processes may be favourable to diamond growth. The key species are CH_3 radicals [194, 195]; they are adsorbed on a surface site, left free after H_2 formation by recombination of an atom impinging from the plasma with an ad-atom, and the carbon atom is incorporated in the crystallographic structure.

Needing thick layers, large growth rates must be associated to a high crystallographic quality. To reach this result, one should be able to produce a large amount of hydrogen atoms into the plasma phase, and then to transport them up to the diamond surface. As a matter of fact, the CH_3-radical adsorption process occurs 10^{-4} times slower than H-atom.

One needs to understand clearly the processes occurring into the plasma phase as well as at the plasma-surface interface. In addition to that, one must be concerned by the definition of the microwave cavity that will determine the plasma stability and the homogene-

ity of the local parameter distributions at the plasma/surface interface. Since in most of the reactors, diamond deposition is mainly limited by H-atom diffusion, the area onto which diamond is deposited as well as the diamond thickness uniformity are directly related to the ability in producing a uniform hydrogen atom density near the growing diamond surface. In microwave cavity-based reactors, the area onto which diamond can be deposited is defined by the microwave wavelength. Decreasing the frequency from 2.45 GHz to 915 MHz provides an alternative to increase up to 6 inches the maximum deposition diameter [196]. Cleanness, gas purity, deposition area, substrate temperature must be controlled in order to grow high purity/high quality diamond single crystals.

6.1 Growing diamond in a plasma

6.1.1 Growth rate and active species

As reported by Goodwin [194, 195] in his well-known papers of 1993 focused on diamond growth mechanisms on (100) faces, CH_3 radicals and H atoms are the key parameters. A rather simple growth law was deduced however only valid for CH_3 radical and H-atom densities in the range of $[3 \times 10^{-10}, 10^{-5}]$ mole/cm^3 and $[10^{-11}, 10^{-6}]$ mole/cm^3 respectively:

$$V_g = \frac{k(T_s)[CH_3]_s \cdot [H]_s}{5 \times 10^{-9} + [H]_s} \tag{53}$$

where $k(T_s)$ is the rate constant and T_s is the surface temperature. $k(T_s) = 1.8 \times 10^{11}$ at surface temperature $T_s = 1200$ K and, $[H]s$ and $[CH_3]s$ are the densities of surface H-atom and CH_3-radical (in mole/cm^3) respectively and V_g is the growth rate. From Eq. 53, it comes clearly that, to increase growth rate, one can increase the surface density/flux of either H-atom or CH_3-radical, or both simultaneously.

LSPM [197–200] as well as the University of Bristol [201–203], have been working for many years to analyze diamond growth plasmas by means of modelling, spectroscopy [204, 205] and measurements of diamond growth rates and quality.

To estimate the best way to improve growth rates, one must identify not only how and where H atoms and CH_3 radicals are produced into the gas phase, but also how they can be lost in the gas phase and how they are transported towards the diamond surface [189]. Then, the capability in increasing the H-atom and CH_3-radical densities (or fluxes) at the surface proceeds from the understanding of the chemical processes occurring into the plasma and at the plasma/surface interface, both locations constitute the engine of production of the right species.

6.1.2 How does the plasma works

Let us consider a diamond plasma reactor operating under moderate pressure conditions in a microwave (MW) cavity coupling based reactor [206, 207]. The gas activation is provided by an electrical discharge that results from stationary waves formed between an applicator and the cavity.

Understanding diamond deposition process requires the development of satisfactory H_2/CH_4 plasma models (validated through experimental means) that provide the estimation of the spatial distributions of species densities into the deposition reactor [200]. Due to the strong coupling between the electromagnetic, thermal, chemistry and transport phenomena that take place in the plasma, such models require taking into account the following effects:

1. Excitation wave propagation in the reactor and its interaction with the plasma.
2. Electrons kinetics and its impact on the energy distribution function (eedf) and the thermal non-equilibrium in the plasma.
3. Chemical kinetics, including e-hs (electron-heavy species) and hs-hs collisions in the discharge.
4. Energy transfer between the different energy modes of the plasma.
5. Transport of energy and chemical species in the plasma.
6. Interactions between the plasma species and the diamond surface and the reactor walls.

It appears that a complete modelling of the deposition reactor is in fact very complex, and a step by step approach has been chosen at LSPM from 1990.

According to specific phenomena to be analyzed, specific models have been constructed. In parallel, the experimental validation has been performed progressively [208, 209]. This approach allowed reducing the complexity, before including additional phenomena into the model. A reliable 1D model able to run in H_2/CH_4 with a reasonable computational time has been developed leading to understand, as a function of the conditions, the respective roles of chemical and transport processes that affect diamond deposition.

Thus, it has been shown that at low power density (<15 W/cm^3), the electron impact dissociation plays a significant role, while at high power density (>15 W/cm^3), thermal dissociation remains the only channel for dissociation of molecular hydrogen as well as methane.

A second plasma model, operating in 2D in H_2-CH_4 mixtures and taking into account the buoyancy, has been developed more recently [210, 211].
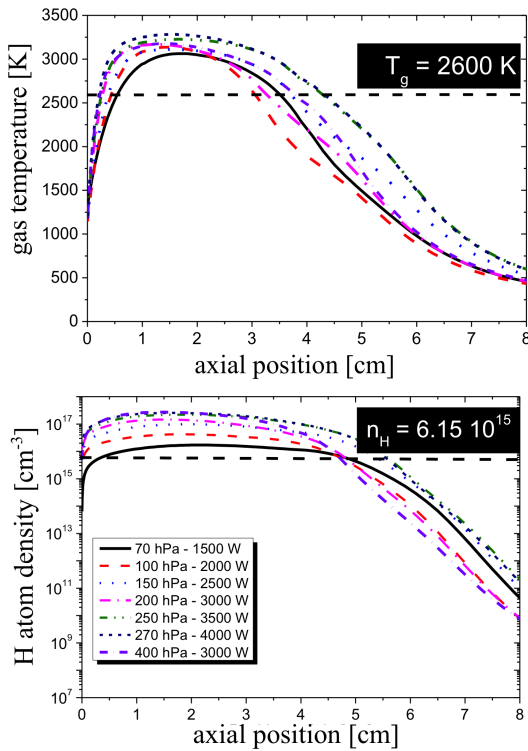
Fig. 33 Spatial distribution of gas temperatures (top) and H-atom densities (bottom) for some power and pressure couples. The reactor is a cylindrical chamber where the plasma, 6 cm in height and 2 inches in diameter, is produced.

### 6.1.3 Main production and loss processes for H atoms and CH₃ radicals

6.1.3 Main production and loss processes for H atoms and CH₃ radicals

The H atoms participate to methane dissociation and CH₃ radical production in volume and at the plasma/ surface interface via

$$H + CH_x \rightleftharpoons CH_{x-1} + H_2 \;\; (x = 3, 4)$$

with $x=3,4$ or

$$H + CH_3 + M \rightarrow CH_4 + M$$
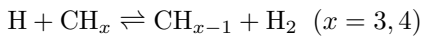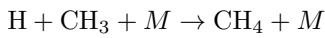
and a set of very fast reactions (see Tab. 3) that occurs at relatively high temperature. These reactions may participate to H-atom loss, in competition to surface reactions such as surface recombination, etching and abstraction processes. Two processes are responsible for the production of H atoms:

$$H_2 + H_2 \rightarrow 2H + H_2$$

$$H_2 + H \rightarrow 3H$$
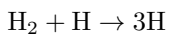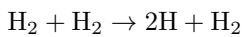
under conditions of high pressure/high MW power. Diffusion towards locations of lower H-atom density ensures an efficient transport of H-atom through the surface boundary layer where they recombine, leaving free adsorption sites where CH₃ radicals may adsorb.

Table 3 Fast equilibrium reactions

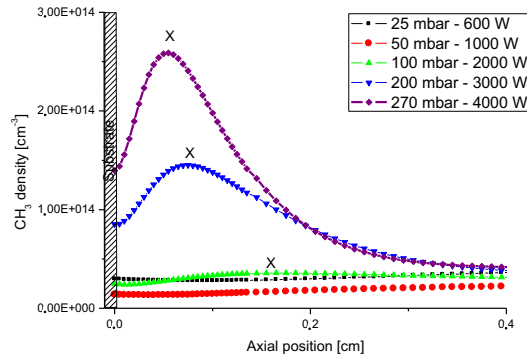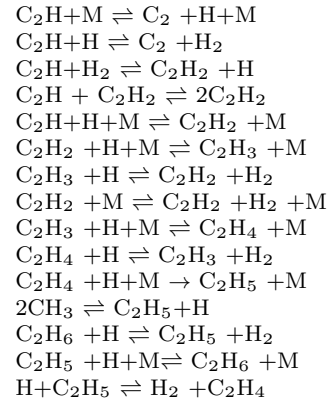| |
|---|
| $C_2H+M \rightleftharpoons C_2 +H+M$ |
| $C_2H+H \rightleftharpoons C_2 +H_2$ |
| $C_2H+H_2 \rightleftharpoons C_2H_2 +H$ |
| $C_2H + C_2H_2 \rightleftharpoons 2C_2H_2$ |
| $C_2H+H+M \rightleftharpoons C_2H_2 +M$ |
| $C_2H_2 +H+M \rightleftharpoons C_2H_3 +M$ |
| $C_2H_3 +H \rightleftharpoons C_2H_2 +H_2$ |
| $C_2H_2 +M \rightleftharpoons C_2H_2 +H_2 +M$ |
| $C_2H_3 +H+M \rightleftharpoons C_2H_4 +M$ |
| $C_2H_4 +H \rightleftharpoons C_2H_3 +H_2$ |
| $C_2H_4 +H+M \rightarrow C_2H_5 +M$ |
| $2CH_3 \rightleftharpoons C_2H_5+H$ |
| $C_2H_6 +H \rightleftharpoons C_2H_5 +H_2$ |
| $C_2H_5 +H+M \rightleftharpoons C_2H_6 +M$ |
| $H+C_2H_5 \rightleftharpoons H_2 +C_2H_4$ |

Fig. 34 Spatial distribution of CH₃-radical density at the plasma/surface interface.

In order to reach high surface H-atom densities, very high gas temperature (3500 K–5000 K) with a maximum peak located very close to the surface are necessary. An increase in power density coupled to the plasma (high pressure and/or power values) was seen to induce both an increase in the maximum value of the gas temperature T_g and a shortening of the distance of this maximum peak relatively to the substrate (Fig. 33top). The same behaviour is observed for H-atom density (Fig. 33bottom).

The axial distributions of T_g and H-atom density control then the CH₃ radical density distribution at the plasma/ surface interface (Fig. 34). It is worth noting that the higher the power density, the higher the gas temperature gradient at the surface, and the higher and closer to the surface the CH₃ density in the near surface interface. The fast reaction set

$$CH_4 + H \rightleftharpoons CH_3 + H_2$$
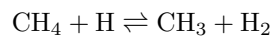
is largely predominant in volume to produce and consume CH₃-radicals , reaching equilibrium. CH₃ radical density appears to be maximum in the near vicinity
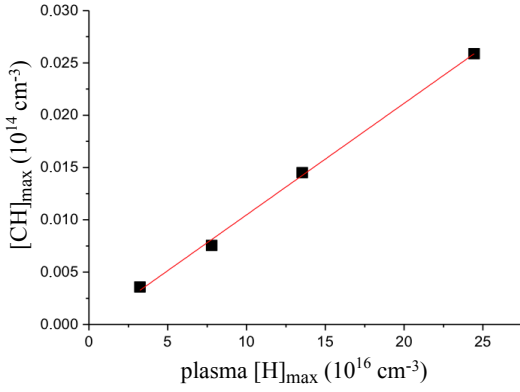
Fig. 35 Variation of CH$_3$-radical density at the surface as a function of H-atom density into the plasma bulk. The x's represent the maximum density obtained for given conditions.

Fig. 36 Variation of the growth rate (in μm/h) as a function of the H-atom density into the plasma bulk according to calculation and measurements.

of the diamond surface where the gas temperature is decreasing and reaches around 1650 K.

The surface CH$_3$ density has been seen to vary linearly with the maximum of CH$_3$ produced at the plasma / surface interface. As CH$_3$ density is by construction linearly dependant of the H-atom density at the location where it is produced and as H-atom density at the surface boundary layer depends linearly on the maximum H-atom density (in the plasma bulk), then we can deduce that a linear relationship links the CH$_3$ density to the maximum of H-atom density into the gas phase (Fig. 34) [189].

6.1.4 Influence of the power and pressure

The ability in coupling high microwave power at high pressure to the plasma is one of the best ways to increase gas temperature and H-atom maximum density as well as to reduce the boundary layer thicknesses. As a consequence, the diamond (100)-face growth rates increase.

The variations of the measured growth rates as a function of the maximum H-atom density measured in the gas phase as well as the variations of growth rates calculated using the growth law established by Harris and Goodwin are reported in Figure 36.

Transforming Eq. 53, it comes:

$$V_g = k(T_s)[CH_3]_s \left(1 + \frac{5 \times 10^{-9}}{[H]_s}\right)^{-1}$$
$$= k(T_s)k'[CH_3]_s \left(1 + \frac{5 \times 10^{-9}}{[H]_s}\right)^{-1} [H]_\infty \tag{54}$$

where k' is a constant that takes into account for the proportionality between the surface CH$_3$ density and the H-atom density in the plasma bulk, for a given CH$_4$ percentage considered, as shown above (Fig. 35).
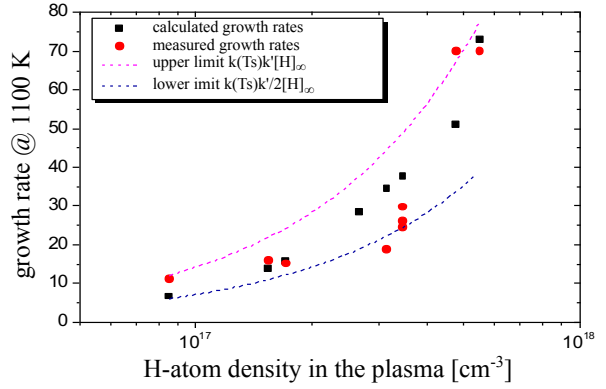
A strong increase in the growth rate is observed once the bulk H-atom density ($[H]_\infty$) is higher than 10^{17} cm^{-3} (or 16×10^{-8} mole/cm^3), and the surface H-atom density ($[H]_s$) higher than around 3×10^{15} cm^{-3} (5×10^{-9} mole/cm^3) (Fig. 36). Recalling for the maximum value predicted by Goodwin of 10^{-6} mole/cm^3, for a fully dissociated plasma running at high velocity and 2 atmospheres, it comes that the growth rate in plasma reactors running in carbon-hydrogen mixture and for power density higher than around 30 W/cm^3 will be included between a lower and an upper value written as it follows:

$$k(T_s)\frac{k'}{2}[H]_\infty < V_g < k(T_s)k'[H]_\infty \tag{55}$$

Taking the proportionality factor of $k' = 6.3 \times 10^{-4}$ corresponding to a percentage of methane of 7%, it come

$$k(T_s)\, 3.15 \times 10^{-4}[H]_\infty < V_g < k(T_s)\, 6.3 \times 10^{-4}[H]_\infty \tag{56}$$

where $[H]_\infty$ is expressed in mole/cm^3. In Figure 36 are plotted the lower and upper limits that border all the measured and calculated growth rates.

6.2 Growing thick diamond for jewelry

Growing diamond for application in jewelry needs growing thick and large diamond layers. Growing thick crystals needs understanding plasma processes to keep identical conditions for the whole duration of growth. Enlarging diamond area can be made either by choosing growth conditions leading to lateral growth or joining carefully seeds together to form a mosaic as proposed by J. Giling and then used by Findeling et al. [212–215].
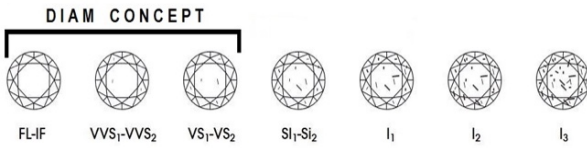
Fig. 37 Simulated inclusions as they may appear under 10× magnification. Labels indicate the conventional scale for decreasing clarity.

Diamonds destined to jewelry are evaluated through the well-known 4 C, *Colour*, *Clarity*, *Carat*, *Cut* (Figure 37). Diamonds' *Colour* is graded from D (colourless or white) to Z (light colour or yellowish). Fancy , i.e. colored, diamonds have a specific classification.

Clarity grade of a diamond quantifies inclusions or blemishes each diamond has and it is ranked on a scale ranging from ÒFlawlessÓ (higher clarity grade) to "Included". 1 *Carat* is the weight of a diamond equal to 0.2 gram. The last C concerns the *Cut* that can be round (brilliant), emerald, princess, cushion, pear É. This criterion takes also into account for the quality of the polishing.

Another graduation concerns the *fancy coloured* diamonds. They are based on atomic impurities incorporated mostly in substitution giving rise to coloured centers in diamond. It happens, however, that diamonds can be brownish due to deformation of their structure while they do not contain any atomic impurities [216, 217].

Extended defects located into the diamond bulk, such as dislocations or non-diamond aggregates, decrease the diamond clarity. Crystal defects may also promote twin formation during growth under plasma conditions.

In most of the plasma reactors, growing diamond without any atomic impurity, such as nitrogen, remains a challenge. This is directly related to the pressure limit of the reactor and to the purity of the gas used. Nitrogen incorporation prevents to reach the highest diamond colours, namely D, E, F, and diamond colour is shifted towards lower grades such as I, J, ... With a variable amount of nitrogen, diamonds may become light to deep brown (champagne to fancy orangy or cognac colours). Nitrogen used as an impurity into the plasma gas mixture enhances the diamond crystallinity as this has been observed by many research groups. Thus, growers often add some molecular nitrogen as impurity. The brownish diamonds are then treated by high pressure - high temperature processes in order to bleach them and obtain white colours (around G). Another method proposed by Element Six limited Company [218] consists in introducing at least two impurities into the plasma, for example in order to combine brownish colour to blue colour into the diamond lattice. Thus, the association of nitrogen and boron into the plasma phase that will incorporated in substitution of some few carbon atoms provides white diamonds. Some key plasma parameters influence the role of nitrogen effect. For instance, increasing the plasma power density coupled to the plasma leads to a higher molecular dissociation, increasing atomic nitrogen density in the gas phase. Another key parameter is the diamond surface temperature that enhances or decreases the effect of incorporation of nitrogen. The higher the temperature, the lower the amount of nitrogen incorporated into the diamond lattice. However, too high temperatures may lead to crystal defect formation during growth. Low growth temperature may improve the diamond quality even in the absence of nitrogen. However, the development of some crystallographic faces may lead to diamond cracks or even breaks. Many groups of researchers are working today on how to produce transparent white (D, E, F) grade diamonds, the type of diamonds preferred by consumers, especially for wedding rings. Thus, experiments with different gas mixtures including oxygen, boron containing species, rare gas, . . . , in addition to molecular hydrogen and methane are currently used in the literature [219].

In Diam Concept, the French diamond grower company, we have worked on the relationship between the colour grading made by the International Gemmological Institute (IGI) in Belgium and the measurements of the ratio of two lines extracted from the photoluminescence analysis using an HR Labram with a laser-wavelength centred at 473 nm. The first line corresponds to the Raman intensity related to the diamond phase (I_D) and the second to incorporation of nitrogen into the diamond lattice (I_{575}). In Fig. 38 is shown a typical photoluminescence spectrum where, one can observe the diamond peak centered at 504.8 nm, the first NV colour centre (N-V0) at 575.5 nm, the second (N-V-) at 638 nm and finally a Si-V colour centre (Si-V) centered at 737.5 nm.

In Fig. 39 it is shown the variation of the ratio I_D/I_{575} as a function of the diamond colour as established by IGI.

The results clearly show that for high nitrogen incorporation (low ratio I_D/I_{575},), deep fancy brown colours are obtained. On the opposite the highest I_D/I_{575}, corresponds to very transparent-white diamonds.

To obtain blue diamonds, introduction of boron containing species such as B_2H_6 into the plasma phase is necessary. As a function of the diborane incorporated into the diamond lattice, light blue to black colours can be obtained as reported in [220].
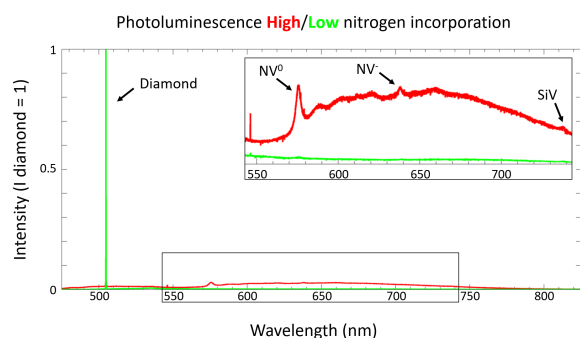
Fig. 38 Typical photoluminescence spectrum revealing the incorporation of nitrogen and silicon atoms into the diamond lattice.
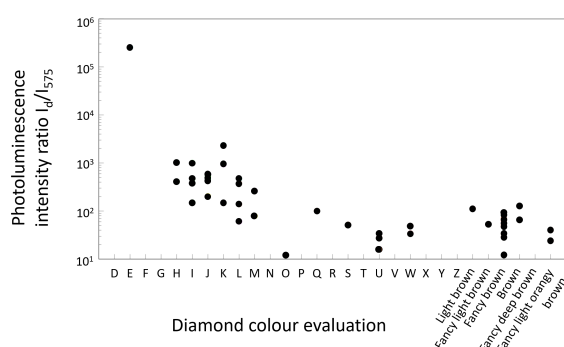

Fig. 39 Ratio of I_D/I_{575}, photoluminescence intensity ratio of plasma CVD diamond over a colour centre due to nitrogen incorporation as a function of the colour evaluation of the diamonds realized by IGI (Belgium).

7 Conclusions

This review presents nowadays research activities ranging from fundamental theoretical aspects to industrial applications of plasmas. In spite of the long history of plasma research, there are still many mechanisms occurring in the plasma that need to be clarified. Large efforts are needed in the next future to cover the gap and the main challenge is to bring together skills coming from physical, chemical, engineering and biological areas, converging in this multidisciplinary research field.

Collisions are responsible of many macroscopic properties, also in conditions when the plasma is usually collisionless. Therefore, accurate collisional data, such as electron impact cross sections and state-resolved rates, are necessary to construct reliable models with predictive capabilities. The plasma composition calculated by models is very sensitive to some of these quantities. Extending gas discharge technology to new mixtures and applications will require strong efforts in constructing the adequate reaction scheme. The growing power of computers allows to model complex plasma configura-

tions, considering also extended reaction schemes. Alternately, efficient sensitivity analysis and reaction reduction procedure can improve the computational costs of the chemical kinetics, with the eventual drawback of limiting the validity region of the reaction model due to the synergy between plasma parameters and chemical processes.

This is the case of DBDs, investigated here by a drift-diffusion model. The results have shown that the overall physics taking place in the gas gap is dominated by the electric charge deposition phenomena. The electrostatic field produced by the deposited charge is responsible for both the external voltage screening during the first and third quarters of each cycle and the observed gap voltage reversal during the second and fourth quarters. The results also suggest that the main contribution to surface charge deposition is provided by the drift velocity. Since the advective fluxes are caused by the electric field, this finding is coherent with the interpretation of the charge deposition acting as a negative feedback with respect to the externally applied electric field.

The theoretical study of DBDs should help in the interpretation of the experimental results in the complex plasma formed in the vicinity of the water surface, where species with high oxidation power, such as ozone and hydrogen peroxides are formed, inducing sanification capabilities against pathogens. Main issues related with this class of discharges are the interactions that occur in the gaseous and liquid phases on the one hand, and the subsequent interactions between active species and charged particles with chemical compounds and living matter on the other hand. Cold plasmas produced in these reactors are usually cost-effective, because they are ignited in atmospheric pressure and require limited energy consumption to be ignited and sustained, due to their non-thermal nature. These discharges trigger a series of chemical reactions able to produce reactive oxygen and nitrogen species because of the presence of air, but also hydrogen reactive species as well.

Interaction of the plasma with the matter is also important in plasma assisted deposition, as in the case of the growth of diamond crystals in MW discharges. This application, apart the technological interest of diamond in electronics, will attract the interest of common people to the plasma, due to the fancy diamonds of large size artificially produced. The possibility to obtaine the desired colour controlling the discharge parameters and buffer gas composition is really attractive.

On the other side, in reactors for nuclear fusion energy production, one of the main issues is to reduce the interaction of the plasma with the surface, in order to reduce the heat load on the reactor, isolating the core,

which is at a temperature of 10^6 K. Nitrogen puffing, dispersing energy through radiation is adequate to this purpose. The injection of N_2 into fusion plasmas for the aim of radiative cooling can have implications owing to the chemical reactivity of N. The most important concerns are connected to modifications of material properties of plasma-facing surfaces and their H_2/D_2 retention characteristics, enhanced erosion of plasma-facing surfaces and production of ammonia. Results obtained during experiments in which W specimens have been exposed at N_2 seeded deuterium plasmas have shown that erosion of the W occur and that surface nitrides are formed. N uptake and W erosion strictly depend on the morphology and nanostructure of the W coatings and from application of the bias potential.

High concentration of ammonia in the exhaust gas stream could compromise overall performance of the divertor. However researches are ongoing to develop more efficient catalysts or alternatives in order to reduce the impurities concentration in waste stream. One of the alternative could be recovery tritium by catalytic decomposition of ammonia previously separate from other impurities, Q_2O, CQ_4, He, CO, CO_2 (Q = H,D,T).

The researches here described are just a drop in the wide variety of plasma applications, illustrating the constant need to bring together different plasma communities. Within that purpose, the course Cold Plasmas: Fundamentals and Applications in the School on Quantum Electronic in Ettore Majorana Center for Scientific Culture in Erice was an excellent opportunity, providing discussions and exchanges about current challenges in plasma physics. Main scope is to bring together skills coming from physical, chemical and biological areas, converging in this multidisciplinary research field.

8 Acknowledgements

9 Authors contributions

Colonna and Pintassilgo managed and organize the contributions. All the authors were involved in the preparation of the manuscript. All the authors have read and approved the final manuscript.

References

1. M.A. Lieberman, A.J. Lichtenberg, *Principles of Plasma Discharges and Materials Processing*, 2nd edn. (Wiley-Interscience, 2005), ISBN 0-471-72001-1
2. G.E. Georghiou, A.P. Papadakis, R. Morrow, A.C. Metaxas, Journal of Physics D: Applied Physics **38**, R303 (2005)
3. J.R. Roth, *Industrial plasma engineering: Volume 2: Applications to nonthermal plasma processing*, Vol. 2 (CRC press, 2001)
4. A. Mizuno, Plasma Physics and Controlled Fusion **49**, A1 (2007)
5. K.H. Becker, U. Kogelschatz, K. Schoenbach, R. Barker, *Non-equilibrium air plasmas at atmospheric pressure* (CRC press, 2004)
6. T. Matsumoto, D. Wang, T. Namihira, H. Akiyama, Air pollution-a comprehensive perspective (2012)
7. B.M. Penetrante, S.E. Schultheis, *Non-thermal plasma techniques for pollution control: part b: electron beam and electrical discharge processing*, Vol. 34 (Springer Science & Business Media, 2013)
8. J. Shang, S. Surzhikov, R. Kimmel, D. Gaitonde, J. Menart, J. Hayes, Progress in Aerospace Sciences **41**, 642 (2005)
9. J.J. Wang, K.S. Choi, L.H. Feng, T.N. Jukes, R.D. Whalley, Progress in Aerospace Sciences **62**, 52 (2013)
10. A.A. Fridman, G.G. Friedman et al., *Plasma medicine* (John Wiley & Sons Chichester, UK:, 2013)
11. M. Laroussi, Plasma processes and polymers **2**, 391 (2005)
12. R. Bickerton, Philosophical Transactions of the Royal Society of London. Series A, Mathematical and Physical Sciences **300**, 475 (1981)
13. F. Pegoraro, P. Veltri, La Rivista del Nuovo Cimento pp. 1–51 (2020)
14. B. Coppi, G. Laval, R. Pellat, Phys. Rev. Lett. **16**, 1207 (1966)
15. R. Kulsrud, H. Furth, E. Valeo, M. Goldhaber, Physical Review Letters **49**, 1248 (1982)
16. R. Kulsrud, E. Valeo, S. Cowley, Nuclear fusion **26**, 1443 (1986)
17. B. Coppi, F. Pegoraro, J.J. Ramos, Phys. Rev. Lett. **51**, 892 (1983)
18. B. Coppi, S. Cowley, R. Kulsrud, P. Detragiache, F. Pegoraro, The Physics of fluids **29**, 4060 (1986)
19. F. Valentini, Journal of Plasma Physics **80**, 529 (2014)
20. J. Pamela, Tech. rep., JET-EFDA Team (2001)
21. J. Rapp, P. Monier-Garbet, G. Matthews, R. Sartori, P. Andrew, P. Dumortier, T. Eich, W. Fundamenski, M. Von Hellermann, J. Hogan et al., Nuclear fusion **44**, 312 (2004)
22. A. Kallenbach, M. Balden, R. Dux, T. Eich, C. Giroud, A. Huber, G. Maddison, M. Mayer, K. McCormick, R. Neu et al., Journal of Nuclear Materials **415**, S19 (2011)
23. J. Rapp, T. Eich, M. Von Hellermann, A. Herrmann, L. Ingesson, S. Jachmich, G. Matthews, V. Philipps, G. Saibene et al., Plasma Physics and Controlled Fusion **44**, 639 (2002)
24. A. Kallenbach, R. Dux, J.C. Fuchs, R. Fischer, B. Geiger, L. Giannone, A. Herrmann, T. Lunt, V. Mertens, R. McDermott et al., Plasma Physics and Controlled Fusion **52**, 055002 (2010)
25. A. Jaervinen, M. Groth, M. Airila, P. Belo, M. Beurskens, S. Brezinsek, M. Clever, G. Corrigan, S. Devaux, P. Drewelow et al., Journal of Nuclear Materials **463**, 135 (2015)

26. M. Oberkofler, G. Meisl, A. Hakola, A. Drenik, D. Ale-gre, S. Brezinsek, R. Craven, T. Dittmar, T. Keenan, S.G. Romanelli et al., Physica Scripta **2016**, 014077 (2016)

27. T. Body, S. Cousens, J. Kirby, C. Corr, Plasma Physics and Controlled Fusion **60**, 075011 (2018)

28. V. Rohde, D. Neuwirth, M. Oberkofler, T. Schwarz-Selinger et al., Balance **20**, 10 (2013)

29. C. Day, B. Butler, T. Giegerich, P. Lang, R. Lawless, B. Meszaros, Fusion Engineering and Design **109**, 299 (2016)

30. C.S. Pitcher, P.C. Stangeby, Plasma Physics and Controlled Fusion **39**, 779 (1997)

31. I. Basis, *Power and Particle Control Nucl*, in *Fusion* (1999), Vol. 39, p. 2391

32. A. Loarte, B. Lipschultz, A. Kukushkin, G. Matthews, P. Stangeby, N. Asakura, G. Counsell, G. Federici, A. Kallenbach, K. Krieger et al., Nuclear Fusion **47**, S203 (2007)

33. T.W. Petrie, D. Buchenauer, D.N. Hill, C. Klepper, S. Allen, R. Campbell, A. Futch, R.J. Groebner, A. Leonard, S. Lippmann et al., Journal of nuclear materials **196**, 848 (1992)

34. M.E. Fenstermacher, J. Boedo, R. Isler, A.W. Leonard, G.D. Porter, D.G. Whyte, R.D. Wood, S. Allen, N.H. Brooks, R. Colchin et al., Plasma physics and controlled fusion **41**, A345 (1999)

35. J. Ongena, A. Messiaen, M. Tokar, U. Samm, B. Unter-berg, N. Schoon, P. Dumortier, H.G. Esser, F. Durodie, H. Euringer et al., Physica Scripta **52**, 449 (1995)

36. W. Eckstein, J. Bohdansky, J. Roth, Nucl. Fusion **1**, 51 (1991)

37. U. Samm, G. Bertschinger, P. Bogen, J. Hey, E. Hintz, L. Konen, Y. Lie, A. Pospieszczyk, D. Rusbuldt, R. Schorn et al., Plasma physics and controlled fusion **35**, B167 (1993)

38. M.Z. Tokar, Fusion Science and Technology **61**, 213 (2012)

39. L. Casali, E. Fable, R. Dux, F. Ryter, ASDEX Upgrade Team, Physics of Plasmas **25**, 032506 (2018)

40. H. Zohm, Plasma Physics and Controlled Fusion **38**, 105 (1996)

41. L. Casali, M. Bernert, R. Dux, R. Fischer, A. Kallen-bach, B. Kurzan, P. Lang, A. Mlynek, R. McDermott, F. Ryter et al., *Transport analysis of high radiation and high density plasmas in the ASDEX Upgrade tokamak*, in *EPJ Web of Conferences* (EDP Sciences, 2014), Vol. 79, p. 01007

42. T. Eich, A.W. Leonard, R.A. Pitts, W. Fundamen-ski, R.J. Goldston, T.K. Gray, A. Herrmann, A. Kirk, A. Kallenbach, O. Kardaun et al., Nuclear fusion **53**, 093031 (2013)

43. M. Bernert, M. Wischmeier, A. Huber, F. Reimold, B. Lipschultz, C. Lowry, S. Brezinsek, R. Dux, T. Eich, A. Kallenbach et al., Nuclear Materials and Energy **12**, 111 (2017)

44. A. Kallenbach, M. Bernert, T. Eich, J. Fuchs, L. Gian-none, A. Herrmann, J. Schweinzer, W.T. and, Nuclear Fusion **52**, 122003 (2012)

45. H. Urano, M. Nakata, N. Aiba, H. Kubo, M. Honda, N. Hayashi, M. Yoshida, Y.K. and, Nuclear Fusion **55**, 033010 (2015)

46. R. Perillo, R. Chandra, G. Akkermans, W.A.J. Vijvers, W.A.A.D. Graef, I.G.J. Classen, J. Van Dijk, M.R. de Baar, Plasma Physics and Controlled Fusion **60**, 105004 (2018)

47. A. Kreter, C. Brandt, A. Huber, S. Kraus, S. Möller, M. Reinhart, B. Schweer, G. Sergienko, B. Unterberg, Fusion science and technology **68**, 8 (2015)

48. A. Kreter, D. Nishijima, R.P. Doerner, M. Freisinger, C. Linsmeier, Y. Martynova, S. Möller, M. Rasinski, M. Reinhart, A. Terra et al., Nuclear fusion **59**, 086029 (2019)

49. A. Uccello, F. Ghezzi, L. Laguardia, R. Caniello, D. Dellasega, F. Dell'Era, D. Della Torre, R. Donnini, G. Granucci, E. Mesto et al., Nuclear Materials and En-ergy **25**, 100808 (2020)

50. L. Laguardia, R. Caniello, A. Cremona, D. Del-lasega, F. Dell'Era, F. Ghezzi, G. Gittini, G. Granucci, V. Mellera, D. Minelli et al., Journal of Nuclear Mate-rials **463**, 680 (2015)

51. D. Ricci, A. Cremona, S. Garavaglia, G. Granucci, D. Iraji, M. Lontano, V. Mellera, D. Minelli, *Experi-mental characterization of instabilities in the linear device GyM*, in *Proc. of the 39th EPS Conference, Stockholm, Sweden, ECA* (2012), Vol. 36

52. L. Laguardia, R. Caniello, A. Cremona, G. Gatto, G. Gervasini, F. Ghezzi, G. Granucci, V. Mellera, D. Minelli, R. Negrotti et al., Nuclear materials and Energy **12**, 261 (2017)

53. H. Kiyooka, O. Matsumoto, Plasma chemistry and plasma processing **16**, 547 (1996)

54. E. Carrasco, M. Jiménez-Redondo, I. Tanarro, V.J. Her-rero, Physical Chemistry Chemical Physics **13**, 19561 (2011)

55. R.J. Donovan, D. Husain, Chemical Reviews **70**, 489 (1970)

56. B.D. Green, G.E. Caledonia, The Journal of Chemical Physics **77**, 3821 (1982)

57. H.L. Chen, H.M. Lee, S.H. Chen, Y. Chao, M.B. Chang, Applied Catalysis B: Environmental **85**, 1 (2008)

58. R.P. Doerner, M.J. Baldwin, M. Simmonds, J.H. Yu, L. Buzi, T. Schwarz-Selinger, Nuclear Materials and En-ergy **12**, 372 (2017)

59. O.Y. Kolesnychenko, O.I. Shklyarevskii, H. Van Kem-pen, Physica B: Condensed Matter **284**, 1257 (2000)

60. Y.C. Chen, J.E. Cunningham, C.P. Flynn, Physical Re-view B **30**, 7317 (1984)

61. O.J. Bchir, K.C. Kim, T.J. Anderson, V. Craciun, B.C. Brooks, L. McElwee-White, Journal of The Electro-chemical Society **151**, G697 (2004)

62. I. Tajima, M. Yamamoto, Journal of Polymer Science Part A: Polymer Chemistry **25**, 1737 (1987)

63. M.B. Yaala, L. Marot, R. Steiner, L. Moser, G. De Tem-merman, C. Porosnicu, C.P. Lungu, M. Oberkofler, E. Meyer, Nuclear Fusion **58**, 106012 (2018)

64. G. Colonna, in *Plasma Modeling: Methods and Applica-tions*, edited by G. Colonna, A. D'Angola (IOP Pub-lishing, 2016), chap. 1

65. D. Kremp, M. Schlanges, W.D. Kraeft, *Quantum Statis-tics of Nonideal Plasmas*, Atomic, Optical and Plasma Physics (Springer, 2005)

66. K. Roussel, R. O'connell, Physical Review A **9**, 52 (1974)

67. G. Colonna, A. Laricchiuta, Entropy **22**, 237 (2020)

68. A. Laricchiuta, G. Colonna, M. Capitelli, A. Kosarim, B.M. Smirnov, The European Physical Journal D **71**, 1 (2017)

69. G. Capriati, G. Colonna, C. Gorse, M. Capitelli, Plasma Chemistry and Plasma Processing **12**, 237 (1992)

70. G. Colonna, A. D'Angola, in *Plasma Modeling: Methods and Applications*, edited by G. Colonna, A. D'Angola (IOP Publishing, 2016), chap. 2

71. D. Loffhagen, in *Plasma Modeling: Methods and Applications*, edited by G. Colonna, A. D'Angola (IOP Publishing, 2016), chap. 3

72. J. Stephens, Journal of Physics D: Applied Physics **51**, 125203 (2018)

73. S. Swanekamp, P. Ottinger, P. Adamson, J. Giuliani, T.B. Petrova, A. Richardson, I. Rittersdorf, Physics of Plasmas **26**, 103506 (2019)

74. S. Longo, Plasma Sources Science and Technology **9**, 468 (2000)

75. R. Winkler, D. Loffhagen, F. Sigeneger, Applied Surface Science **192**, 50 (2002), advance in Low Temperature RF Plasmas

76. S.D. Rockwood, Phys. Rev. Lett. **8**, 2348 (1973)

77. M.A. Ridenti, V. Guerra, J. Amorim, in *Plasma Modeling: Methods and Applications*, edited by G. Colonna, A. D'Angola (Institute of Physics, 2016), IOP Plasma Physics, chap. 11

78. M. Mitchner, C.H. Kruger, Wiley Series in Plasma Physics, J. Wiley and Sons, New York (1973)

79. I. Simonović, D. Bošnjaković, Z.L. Petrović, P. Stokes, R. White, S. Dujko, Physical Review E **101**, 023203 (2020)

80. I. Simonović, D. Bošnjaković, Z.L. Petrović, R.D. White, S. Dujko, The European Physical Journal D **74**, 1 (2020)

81. A. Tejero-del Caz, V. Guerra, D. Gonçalves, M.L. da Silva, L. Marques, N. Pinhao, C. Pintassilgo, L. Alves, Plasma Sources Science and Technology **28**, 043001 (2019)

82. G.J.M. Hagelaar, L.C. Pitchford, Plasma Sources Science and Technology **14**, 722 (2005)

83. S. Rassou, D. Packan, J. Labaune, Physics of Plasmas **24**, 100704 (2017)

84. J. Levaton, A.N. Klein, J. de Amorim, C. Binder, Plasma Research Express **1**, 045004 (2019)

85. X. Chen, L. Lan, H. Lu, Y. Wang, X. Wen, X. Du, W. He, Journal of Physics D: Applied Physics **50**, 395202 (2017)

86. C.J. Peters, M.N. Shneider, R.B. Miles, Journal of Applied Physics **125**, 243301 (2019)

87. P.J. Drallos, V.P. Nagorny, W. Williamson, Plasma Sources Science and Technology **4**, 576 (1995)

88. G.K. Grubert, M.M. Becker, D. Loffhagen, Phys. Rev. E **80**, 036405 (2009)

89. G. Colonna, L.D. Pietanza, G. D'Ammando, in *Plasma Modeling: Methods and Applications*, edited by G. Colonna, A. D'Angola (IOP Publishing, 2016), chap. 8

90. M. Capitelli, G. Colonna, F. Esposito, K. Hassouni, A. Laricchiuta, S. Longo, *Fundamental Aspects of Plasma Chemical Physics: Kinetics* (Springer, 2015)

91. M. Capitelli, I. Armenise, E. Bisceglie, D. Bruno, R. Celiberto, G. D'Ammando, O. De Pascale, F. Esposito, C. Gorse, V. Laporta et al., Plasma Chemistry and Plasma Processing **32**, 427 (2012)

92. M. Capitelli, I. Armenise, D. Bruno, M. Cacciatore, R. Celiberto, G. Colonna, O. De Pascale, P. Diomede, F. Esposito, C. Gorse et al., Plasma Sources Science and Technology **16**, S30 (2007)

93. J. Amorim, M. Ridenti, V. Guerra, Plasma Physics and Controlled Fusion **57**, 074001 (2015)

94. M.A. Ridenti, J. de Amorim, A. Dal Pino, V. Guerra, G. Petrov, Phys. Rev. E **97**, 013201 (2018)

95. C. Yuan, Z. Zhou, J. Yao, E.A. Bogdanov, A.A. Kudryavtsev, K.M. Rabadanov, Plasma Sources Science and Technology **28**, 035017 (2019)

96. C.D. Pintassilgo, V. Guerra, Plasma Sources Science and Technology **26**, 055001 (2017)

97. W. Yang, Q. Zhou, Z. Dong, AIP Advances **6**, 055209 (2016)

98. M. Hübner, S. Gortschakow, O. Guaitella, D. Marinov, A. Rousseau, J. Röpcke, D. Loffhagen, Plasma Sources Science and Technology **25**, 035005 (2016)

99. C.D. Pintassilgo, V. Guerra, Plasma Physics and Controlled Fusion **61**, 014026 (2018)

100. W. Yang, Q. Zhou, Z. Dong, E. Yan, Physics of Plasmas **26**, 073512 (2019)

101. G. Colonna, V. Laporta, R. Celiberto, M. Capitelli, J. Tennyson, Plasma Sources Science and Technology **24**, 035004 (2015)

102. G. Colonna, G. D'Ammando, L. Pietanza, Plasma Sources Science and Technology **25**, 054001 (2016)

103. N. Dyatko, Y.Z. Ionikh, A. Meshchanov, A. Napartovich, Plasma Physics Reports **44**, 334 (2018)

104. M. Hannemann, P. Hardt, D. Loffhagen, M. Schmidt, R. Winkler, Plasma Sources Science and Technology **9**, 387 (2000)

105. D. Loffhagen, M.M. Becker, A.K. Czerny, J. Philipp, C.P. Klages, Contributions to Plasma Physics **58**, 337 (2018)

106. G. Colonna, A. Laricchiuta, L.D. Pietanza, Plasma Physics and Controlled Fusion **62**, 014003 (2020)

107. S. Sharma, N. Sirse, M. Turner, A. Ellingboe, Physics of Plasmas **25**, 063501 (2018)

108. L. Pietanza, G. Colonna, M. Capitelli, Physics of Plasmas **27**, 093510 (2020)

109. G. Colonna, L.D. Pietanza, G. D'Ammando, R. Celiberto, M. Capitelli, A. Laricchiuta, The European Physical Journal D **71**, 1 (2017)

110. G. Hartmann, I. Gallimberti, Journal of Physics D: Applied Physics **8**, 670 (1975)

111. M. Capitelli, M. Dilonardo, Zeitschrift für Naturforschung A **34**, 585 (1979)

112. M. Capitelli, C. Gorse, M. Berardini, G. Braglia, Lettere al Nuovo Cimento **31**, 231 (1981)

113. M. Capitelli, C. Gorse, A. Ricard, Journal de Physique Lettres **42**, 469 (1981)

114. M. Capitelli, M. Dilonardo, R. Winkler, J. Wilhelm, Beiträge aus der Plasmaphysik **26**, 443 (1986)

115. M. Capitelli, G. Colonna, K. Hassouni, A. Gicquel, Chemical Physics Letters **228**, 687 (1994)

116. G. D'Ammando, G. Colonna, M. Capitelli, A. Laricchiuta, Physics of Plasmas **22**, 034501 (2015)

117. G. Colonna, M. Capitelli, S. DeBenedictis, C. Gorse, F. Paniccia, Contributions to Plasma Physics **31**, 575 (1991)

118. G. Colonna, C. Gorse, M. Capitelli, R. Winkler, J. Wilhelm, Chemical Physics Letters **213**, 5 (1993)

119. G. Colonna, M. Capitelli, Journal of Physics D: Applied Physics **34**, 1812 (2001)

120. G. Colonna, Plasma Sources Science and Technology **29**, 065008 (2020)

121. N.A. Popov, Journal of Physics D: Applied Physics **44**, 285201 (2011)

122. V. Guerra, P. Sá, J. Loureiro, The European Physical Journal-Applied Physics **28**, 125 (2004)

123. V. Guerra, P.A. Sá, J. Loureiro, Plasma Sources Science and Technology **12**, S8 (2003)

124. I. Shkurenkov, I.V. Adamovich, Plasma Sources Science and Technology **25**, 015021 (2016)

125. J. Loureiro, C.M. Ferreira, Journal of Physics D: Applied Physics **19**, 17 (1986)

126. I.N. Kadochnikov, I.V. Arsentiev, Journal of Physics D: Applied Physics **51**, 374001 (2018)
127. Q. Hong, X. Wang, Y. Hu, Q. Sun, Physics of Fluids **32**, 046102 (2020)
128. M. Capitelli, C.M. Ferreira, B.F. Gordiets, A.I. Osipov, *Plasma kinetics in atmospheric gases*, Vol. 31 (Springer Science & Business Media, 2013)
129. F. Krcma, V. Mazánková, I. Soural, V. Guerra, IEEE Transactions on Plasma Science **42**, 2384 (2014)
130. U. Kogelschatz, Plasma Chemistry and Plasma Processing **23** (2003)
131. A. Fridman, A. Chirokov, A. Gutsol, Journal of Physics D: Applied Physics **38**, R1 (2005)
132. A. Cristofolini, A. Popoli, *A multi-stage approach for DBD modelling*, in *Journal of Physics: Conference Series* (IOP Publishing, 2019), Vol. 1243, p. 012012
133. R. Brandenburg, Plasma Sources Science and Technology **26**, 053001 (2017)
134. A. Cristofolini, G. Neretti, A. Popoli, A. Ricchiuto, P. Seri, *Experimental and Numerical Investigation on the Electric Charge Deposition in a Dielectric Barrier Discharge*, in *2019 IEEE Conference on Electrical Insulation and Dielectric Phenomena (CEIDP)* (IEEE, 2019), pp. 690–693
135. D. de G. ALLEN, The Quarterly Journal of Mechanics and Applied Mathematics **15**, 11 (1962)
136. C. Punset, S. Cany, J.P. Boeuf, Journal of Applied Physics **86** (1999)
137. D.L. Scharfetter, H.K. Gummel, IEEE Transactions on electron devices **16**, 64 (1969)
138. B. Parent, S.O. Macheret, M.N. Shneider, Journal of Computational Physics **259**, 51 (2014)
139. G. Sinnott, D. Golden, R. Varney, Physical Review **170**, 272 (1968)
140. Y. Gosho, A. Harada, Journal of Physics D: Applied Physics **16**, 1159 (1983)
141. I.S. Grigoriev, E.Z. Meæilikhov, *Handbook of physical quantities* (CRC Press, 1997)
142. I. Kossyi, A.Y. Kostinsky, A. Matveyev, V. Silakov, Plasma Sources Science and Technology **1**, 207 (1992)
143. A. Cristofolini, A. Popoli, G. Neretti, International Journal of Applied Electromagnetics and Mechanics **63**, S21 (2020), publisher: IOS Press
144. J.F. Thompson, B.K. Soni, N.P. Weatherill, *Handbook of grid generation* (CRC press, 1998)
145. D. Nikandrovand, L. Tsendin, R. Arslanbekov, V. Kolobov, *Dynamics of ionization fronts during high-pressure gas breakdown*, in *Proceedings of the 59th Annual Gaseous Electronics Conference, vol. SRP2, Columbus, OH* (2006), p. 31
146. S. Pancheshnyi, P. Ségur, J. Capeillère, A. Bourdon, Journal of Computational Physics **227**, 6574 (2008)
147. W.G. Min, H.S. Kim, S.H. Lee, S.Y. Hahn, IEEE transactions on magnetics **37**, 3141 (2001)
148. F. Massines, A. Rabehi, P. Decomps, R.B. Gadri, P. Ségur, C. Mayoux, Journal of Applied Physics **83**, 2950 (1998)
149. F. Peeters, T. Butterworth, in *Atmospheric Pressure Plasma-from Diagnostics to Applications* (IntechOpen, 2018)
150. E.G. Zhuk, Gig. Sanit **38**, 8 (1973)
151. D.M. Willberg, P.S. Lang, R.H. Höchemer, A. Kratel, M.R. Hoffmann, Environmental Science & Technology **30**, 2526 (1996), https://doi.org/10.1021/es950850s
152. P. Sunka, V. Babický, M. Clupek, P. Lukes, M. Simek, J. Schmidt, M. Cernák, Plasma Sources Science and Technology **8**, 258 (1999)
153. H. Akiyama, IEEE Transactions on Dielectrics and Electrical Insulation **7**, 646 (2000)
154. P. Bruggeman, C. Leys, Journal of Physics D: Applied Physics **42**, 053001 (2009)
155. P. Bruggeman, J.V. Slycken, J. Degroote, J. Vierendeels, P. Verleysen, C. Leys, IEEE Transactions on Plasma Science **36**, 1138 (2008)
156. T. Sugimoto, K. Asano, Y. Higashiyama, Journal of Electrostatics **53**, 25 (2001)
157. J.A. Robinson, M.A. Bergougnou, G.S.P. Castle, I.I. Inculet, IEEE Transactions on Industry Applications **37**, 735 (2001)
158. P. Bruggeman, L. Graham, J. Degroote, J. Vierendeels, C. Leys, Journal of Physics D: Applied Physics **40**, 4779 (2007)
159. Y. Miyazaki, K. Satoh, H. Itoh, IEEJ Transactions on Fundamentals and Materials **128**, 172 (2008)
160. Y. Hu, Y. Bai, X. Li, J. Chen, Separation and Purification Technology **120**, 191 (2013)
161. P. Baroch, N. Saito, O. Takai, Journal of Physics D: Applied Physics **41**, 085207 (2008)
162. J. Janca, S. Kuzmin, A. Maximov, J. Titova, A. Czernichowski, Plasma chemistry and plasma processing **19**, 53 (1999)
163. J.L. Brisset, D. Moussa, A. Doubla, E. Hnatiuc, B. Hnatiuc, G. Kamgang Youbi, J.M. Herry, M. Naitali, M.N. Bellon-Fontaine, Industrial & Engineering Chemistry Research **47**, 5761 (2008)
164. S. Gershman, O. Mozgina, A. Belkind, K. Becker, E. Kunhardt, Contributions to Plasma Physics **47**, 19 (2007)
165. P. Seri, A. Wright, A. Shaw, F. Iza, H. Bandulasena, C.A. Borghi, G. Neretti, Plasma Sources Science and Technology **28**, 035001 (2019)
166. P. Lukes, B.R. Locke, Journal of Physics D: Applied Physics **38**, 4074 (2005)
167. F. Tampieri, A. Giardina, F.J. Bosi, A. Pavanello, E. Marotta, B. Zaniol, G. Neretti, C. Paradisi, Plasma Processes and Polymers **15**, 1700207 (2018)
168. P. Lukes, B.R. Locke, Industrial & engineering chemistry research **44**, 2921 (2005)
169. A. Sakudo, Y. Yagyu, T. Onodera, International journal of molecular sciences **20**, 5216 (2019)
170. R. Thirumdas, A. Kothakota, U. Annapure, K. Siliveru, R. Blundell, R. Gatt, V.P. Valdramidis, Trends in food science & technology **77**, 21 (2018)
171. P. Bruggeman, M.J. Kushner, B.R. Locke, J.G. Gardeniers, W. Graham, D.B. Graves, R. Hofman-Caris, D. Maric, J.P. Reid, E. Ceriani et al., Plasma sources science and technology **25**, 053002 (2016)
172. E. Tsoukou, P. Bourke, D. Boehm, Water **12**, 3021 (2020)
173. G. Neretti, M. Taglioli, G. Colonna, C. Borghi, Plasma Sources Science and Technology **26**, 015013 (2016)
174. L. Dong, Y. Zhang, W. Liu, L. Yang, J. Chen, Applied Physics Letters **94**, 091502 (2009)
175. J.H. Choi, T.I. Lee, I. Han, H.K. Baik, K.M. Song, Y.S. Lim, E.S. Lee, Plasma Sources Science and Technology **15**, 416 (2006)
176. M. Capitelli, G. Colonna, O. De Pascale, C. Gorse, K. Hassouni, S. Longo, Plasma Sources Science and Technology **18**, 014014 (2008)
177. M. Capitelli, G. Colonna, G. D'Ammando, V. Laporta, A. Laricchiuta, Physics of Plasmas **20**, 101609 (2013)
178. G. Hagelaar, L. Pitchford, Plasma Sources Science and Technology **14**, 722 (2005)

179. C. Laux, VKI LS Course on hypersonic entry and cruise vehicles, Palo Alto, California, USA (2008)
180. G. Neretti, A. Cristofolini, C.A. Borghi, A. Gurioli, R. Pertile, IEEE Transactions on Plasma Science **40**, 1678 (2012)
181. P. Bruggeman, N. Sadeghi, D. Schram, V. Linss, Plasma Sources Science and Technology **23**, 023001 (2014)
182. J. Majewski, Prz Elektrotech (Electr Rev) **88**, 253 (2012)
183. B.R. Locke, K.Y. Shih, Plasma Sources Science and Technology **20**, 034006 (2011)
184. E. EFSA, EFSA Journal **12**, 3547 (2014)
185. G. Neretti, B. Morandi, M. Taglioli, G. Poglayen, R. Galuppi, G. Tosi, C.A. Borghi, Plasma Medicine **8** (2018)
186. A. Acín, I. Bloch, H. Buhrman, T. Calarco, C. Eichler, J. Eisert, D. Esteve, N. Gisin, S.J. Glaser, F. Jelezko et al., New Journal of Physics **20**, 080201 (2018)
187. M. Lesik, J.P. Tetienne, A. Tallaire, J. Achard, V. Mille, A. Gicquel, J.F. Roch, V. Jacques, Applied Physics Letters **104**, 113107 (2014)
188. A. Tallaire, J. Achard, F. Silva, O. Brinza, A. Gicquel, Comptes rendus physique **14**, 169 (2013)
189. A. Gicquel, F. Silva, C. Rond, N. Derkaoui, O. Brinza, J. Achard, G. Lombardi, A. Tallaire, A. Michau, M. Wartel et al., *Ultrafast Deposition of Diamond by Plasma-Enhanced CVD*, in *Comprehensive hard materials*, edited by Springer (2014), Vol. 3, pp. 217–268
190. J.C. Angus, A. Argoitia, R. Gat, Z. Li, M. Sunkara, L. Wang, Y. Wang, Philosophical Transactions of the Royal Society of London. Series A: Physical and Engineering Sciences **342**, 195 (1993)
191. S.J. Harris, Applied physics letters **56**, 2298 (1990)
192. E. Kondoh, T. Ohta, T. Mitomo, K. Ohtsuka, Journal of applied physics **73**, 3041 (1993)
193. W.L. Hsu, Journal of applied physics **72**, 3102 (1992)
194. D.G. Goodwin, Journal of Applied Physics **74**, 6888 (1993)
195. D. Goodwin, Journal of applied physics **74**, 6895 (1993)
196. M. Füner, C. Wild, P. Koidl, Applied Physics Letters **72**, 1149 (1998)
197. K. Hassouni, T. Grotjohn, A. Gicquel, Journal of Applied Physics **86**, 134 (1999)
198. F. Silva, K. Hassouni, X. Bonnin, A. Gicquel, Journal of physics: condensed matter **21**, 364202 (2009)
199. A. Gicquel, K. Hassouni, S. Farhat, Y. Breton, C. Scott, M. Lefebvre, M. Pealat, Diamond and Related Materials **3**, 581 (1994)
200. K. Hassouni, F. Silva, A. Gicquel, Journal of Physics D: Applied Physics **43**, 153001 (2010)
201. Y.A. Mankelevich, A. Rakhimov, N. Suetin, Diamond and related materials **4**, 1065 (1995)
202. Y.A. Mankelevich, M.N. Ashfold, J. Ma, Journal of applied physics **104**, 113304 (2008)
203. J. Butler, Y.A. Mankelevich, A. Cheesman, J. Ma, M. Ashfold, Journal of Physics: Condensed Matter **21**, 364201 (2009)
204. A. Gicquel, M. Chenevier, K. Hassouni, A. Tserepi, M. Dubus, Journal of applied physics **83**, 7504 (1998)
205. A. Gicquel, M. Chenevier, M. Lefebvre, Handbook of Industrial Diamonds and Diamond Films, ed. MA Prelas, G. Popovici, L. K. Bigelow, Marcel Dekker (1998)
206. A. Gicquel, K. Hassouni, F. Silva, J. Achard, Current Applied Physics **1**, 479 (2001)
207. J. Achard, F. Silva, A. Tallaire, X. Bonnin, G. Lombardi, K. Hassouni, A. Gicquel, Journal of Physics D: Applied Physics **40**, 6175 (2007)
208. G. Lombardi, K. Hassouni, G. Stancu, L. Mechold, J. Röpcke, A. Gicquel, Plasma Sources Science and Technology **14**, 440 (2005)
209. G. Lombardi, G. Stancu, F. Hempel, A. Gicquel, J. Röpcke, Plasma Sources Science and Technology **13**, 27 (2003)
210. S. Prasanna, C. Rond, A. Michau, K. Hassouni, A. Gicquel, Plasma Sources Science and Technology **25**, 045017 (2016)
211. S. Prasanna, A. Michau, C. Rond, K. Hassouni, A. Gicquel, Plasma Sources Science and Technology **26**, 097001 (2017)
212. G. Janssen, L. Giling, Diamond and related materials **4**, 1025 (1995)
213. C. Findeling-Dufour, A. Gicquel, Thin Solid Films **308**, 178 (1997)
214. C. Findeling-Dufour, A. Gicquel, R. Chiron, Diamond and related materials **7**, 986 (1998)
215. C. Findeling-Dufour, A. Vignes, A. Gicquel, Diamond and related materials **4**, 429 (1995)
216. T. Hainschwang, F. Notari, G. Pamies, Minerals **10**, 903 (2020)
217. T. Hainschwang, F. Notari, G. Pamies, Minerals **10**, 914 (2020)
218. S.D. Williams, D.J. Twitchen, P.M. Martineau, G.A. Scarsbrooks, I. Friel, *Wo 2006/136929 a3* (2006)
219. R.J. Hemley, H.K. Mao, C.S. Yan, *Diamond uses/applications based on single-crystal cvd diamond produced at rapid growth rate*, Patent number: 7820131 (2010)
220. J. Achard, F. Silva, R. Issaoui, O. Brinza, A. Tallaire, H. Schneider, K. Isoird, H. Ding, S. Koné, M. Pinault et al., Diamond and Related Materials **20**, 145 (2011)